AFRP20: New P-wavespeed Model for the African Mantle Reveals Two Whole-Mantle Plumes Below East Africa and Neoproterozoic Modification of the Tanzania Craton

A. Boyce[1,2*], I. D. Bastow[1], S. Cottaar[2], R. Kounoudis[1], J. Guilloud De Courbeville[1], E. Caunt[1], S. Desai[1]

[1]Department of Earth Science and Engineering, Royal School of Mines, Prince Consort Road, Imperial College London, London, SW7 2BP, UK.
[2]University of Cambridge, Department of Earth Science, Bullard Laboratories, Madingley Road, Cambridge, CB3 0EZ, UK.

Key Points:

- AFRP20 is an absolute P-wavespeed tomographic model for the African mantle
- AFRP20 reveals two whole-mantle plumes below East Africa
- Slow Tanzanian craton P-wavespeeds reveal Neoproterozoic metasomatic lithospheric modification

*Present Address : University of Cambridge, Department of Earth Science, Bullard Laboratories, Madingley Road, Cambridge, CB3 0EZ, UK.

Corresponding author: Alistair Boyce, ab2568@cam.ac.uk

Abstract

Africa's Cenozoic tectonism is often attributed to mantle plumes, particularly below East Africa, but their morphology, number, location, and impact on the African lithosphere are debated. The broad slow wavespeed African Superplume, ubiquitous in large-scale tomographic models, originates below South Africa, reaching the surface somewhere below East Africa. However, whether the diverse East African mantle geochemistry is best reconciled with one heterogeneous upwelling, or current tomographic models lack the resolution to image multiple distinct plumes, remains enigmatic. S-wavespeed tomographic images of Africa are legion, but higher-frequency P-wavespeed whole-mantle models possessing complementary diagnostic capabilities are comparatively lacking. This hinders attempts to disentangle the effects of Cenozoic hotspot tectonism and Pan African (and older) tectonic events on the East African lithosphere. Here we develop a continental-scale P-wave tomographic model capable of resolving structure from upper-to-lower mantle depths using a recently-developed technique to extract absolute arrival-times from noisy, temporary African seismograph deployments. Shallow-mantle wavespeeds are $\delta V_P \approx$–4% below Ethiopia, but less anomalous ($\delta V_P \geq$–2%) below other volcanic provinces. The heterogeneous African Superplume reaches the upper mantle below the Kenyan plateau. Below Ethiopia/Afar we image a second sub-vertical slow wavespeed anomaly rooted near the core-mantle boundary outside the African LLVP, meaning multiple disparately sourced whole-mantle plumes may influence East African magmatism. In contrast to other African cratons, wavespeeds below Tanzania are only fast to 90–135 km depth. When interpreted alongside Lower Eocene on-craton kimberlites, our results support pervasive metasomatic lithospheric modification caused by subduction during the Neoproterozoic Pan-African orogeny.

Plain Language Summary

The African plate comprises a collage of ancient continental fragments, cratons, over 2.5 billion years old, that have remained largely unchanged since formation. In seismically and volcanically active East Africa, the continent is being broken apart (rifted). Hot mantle rock has been rising slowly from the core-mantle boundary below Africa for millions of years in at least one mantle 'plume'. Seismologists and geochemists often disagree on the number and location of mantle plumes below East Africa, perhaps because geochemical data can be interpreted in multiple ways or seismic images of the mantle are currently not sufficiently detailed to 'see' more than one mantle plume. Given accurate timing of seismic energy arriving from distant earthquakes, 'seismic tomography' can be used to create images of the African mantle. Old tectonic plates, which are cold, usually appear as fast seismic wavespeeds while hot plumes appear as slow wavespeeds. Our new seismic images show two mantle plumes originating in the lower mantle (>2000 km depth) may underlie the volcanoes along the East African Rift valley. Furthermore, by unpicking the signatures of continental assembly from those of younger plumes and rifting origin we reveal surprising evidence for modification of the ancient Tanzanian craton.

AGU "index terms": Africa – Body waves – Tomography – Continental cratons – Hotspots, large igneous provinces, and flood basalt volcanism – Earth's interior: composition and state – Lithosphere

1 Overview

The Cenozoic magmatism, uplift and evolution of the African plate has often been attributed to the presence of mantle upwellings at various scales. In East Africa for example, the number and depth extent of these upwellings is debated (e.g., Furman,

Bryce, et al., 2006; Pik et al., 2006; Rooney, 2017). Tomographic models generally reveal a broad (∼500 km-wide), inclined, slow wavespeed anomaly extending to the core-mantle boundary below South Africa: the African Superplume (e.g., Ritsema et al., 1999; Li et al., 2008). However, more recent models (e.g., Ritsema et al., 2011; Chang et al., 2015) provide tentative evidence for multiple narrower plume tails in the upper mantle, centered below Ethiopia and Kenya. Variability in along-rift isotopic signatures also favor a single heterogeneous lower mantle upwelling, common to and tapped by, multiple upper mantle plume stems (e.g., Furman, Kaleta, et al., 2006; Nelson et al., 2012; Halldórsson et al., 2014). A third interpretation posits that two completely distinct upwellings are required to explain the age distribution and some geochemical characteristics of East African basalts (George et al., 1998; Rogers et al., 2000), but seismic evidence supporting this hypothesis is lacking. Elsewhere, the extent to which Cenozoic intra-plate magmatism in Cameroon and Madagascar requires influence from upwellings sourced below the upper mantle is also uncertain (e.g., King & Ritsema, 2000; French & Romanowicz, 2015; Cucciniello et al., 2017; Pratt et al., 2017).

Sutured during the Pan African orogeny along a series of Paleoproterozoic mobile belts, and now interspersed amongst regions of Cenozoic hotspot tectonism, numerous Archean cratons characterize the African plate. It is thus an ideal place to study the modification of cratonic mantle lithosphere (Figure 1). Subduction/orogenesis, rifting, and hotspot tectonism are all capable of modifying Archean lithosphere (e.g., Wang et al., 2015; Boyce et al., 2016; Liao et al., 2017; Wenker & Beaumont, 2018), but isolating evidence for each process is challenging. Temporal constraints on the development of lithospheric mantle composition can be derived from diamond-bearing kimberlites and mantle xenoliths, but such geological samples are spatially limited across Africa (e.g., Begg et al., 2009). Despite their significant temporal separation, the relative importance of Proterozoic 'Pan African' orogenesis and Cenozoic hotspot tectonism in modifying Africa's Archean mantle lithosphere is therefore uncertain (e.g., Koornneef et al., 2009), meaning concurrent analysis of seismological and xenolith data is essential. For example, the relationship between the edges of fast wavespeed domains and the spatial distribution of African kimberlite magmatism is debated (e.g., Priestley et al., 2008; Begg et al., 2009; Fishwick, 2010; Celli et al., 2020): some authors suggest that a significant portion of thick African lithosphere has been removed, perhaps by recent mantle plume thermal erosion (Celli et al., 2020). In Tanzania specifically, the cratonic lithosphere displays basal topographic asymmetry and is also significantly thinner (∼160 km on average Weeraratne et al., 2003; Adams et al., 2012; O'Donnell et al., 2013; Emry et al., 2019) compared to other cratons worldwide (≥200 km: Lee & Rudnick, 1999; Priestley et al., 2019). On-craton petrological and seismological evidence for Tanzanian craton evolution towards its present-day state is relatively sparse (Stachel et al., 1998; Wölbern et al., 2012). Hence the areal extent, timing and causal mechanism for post-formation modification (e.g., Pan-African subduction, recent Cenozoic hotspot tectonism and/or rifting) remain unresolved (e.g., Koornneef et al., 2009).

While shear waves are sensitive primarily to temperature over composition (in the absence of melt; Goes et al., 2000), compressional wavespeed constraints are a powerful tool to understand lithospheric modification because they have stronger sensitivity to composition. For example, lithospheric modification through metasomatic addition of silica to olivine leads to enrichment in orthopyroxene by water-rock/melt-rock interaction during subduction (e.g., Wagner et al., 2008). This can decrease V_P at mantle lithospheric depths by >1%, with little accompanying impact on V_S and density (Schutt & Lesher, 2010). High resolution African P-wave relative arrival-time studies are abundant (e.g., Fouch et al., 2004; Bastow et al., 2005; Reusch et al., 2010; Mulibo & Nyblade, 2013b), but do not constrain background mean velocity structure; their amplitudes are thus not comparable, or relatable in a consistent way to thermal

and chemical mantle properties (e.g., Bastow, 2012). Global-scale P-wave tomographic models (e.g., Montelli et al., 2006; Simmons et al., 2012; Hosseini et al., 2019) sample long wavelength African mantle structure but are typically tuned to resolve mid-to-lower mantle depths. Continent-scale African absolute P-wave tomographic models are scarce (e.g., Hansen et al., 2012; Hansen & Nyblade, 2013), and none tackle the issue of how to extract absolute arrival-times reliably from temporary seismograph networks, whose short station spacing is required for high resolution lithospheric imaging (Figure 2). The inclusion of data from these networks would also enhance resolution in the lower mantle, pertinent to the aforementioned African plume debates.

Here, we utilize the Absolute Arrival-time Recovery Method (AARM) of Boyce et al. (2017) to embed accurately twenty-five years of data from temporary seismograph networks across Africa (Figure 1) into a new absolute P-wave mantle tomographic model. Our body wave model facilitates direct comparison of slow wavespeed upper mantle structure underlying the Atlas Mountains, the Cameroon Volcanic Line, Madagascar and East Africa. We explore new seismological evidence for two whole-mantle plumes beneath East Africa, sourced at disparate locations at the core-mantle boundary. We also investigate whether Proterozoic (Pan-African) subduction driven modification below the Tanzanian craton can explain its anti-correlated shear and compressional lithospheric wavespeeds.

2 African Mantle Structure and Tectonics

2.1 African Mantle Upwellings

Global tomographic studies consistently reveal a Large Low Velocity Province (LLVP) atop the core-mantle boundary centered below South Africa and the southern Atlantic Ocean (Ritsema et al., 1999; Montelli et al., 2006; Li et al., 2008; Ritsema et al., 2011; Simmons et al., 2012; Chang et al., 2015; Hosseini et al., 2019). From there, a broad, inclined, slow wavespeed feature, often termed the African Superplume, extends upward, reaching the upper mantle somewhere below the East African Rift (e.g., Ni et al., 2002; Simmons et al., 2007; Forte et al., 2010; Hansen et al., 2012). Numerous authors have used converted wave phases in an effort to constrain the composition and temperature of the East African mantle transition zone with possible implications for the development of East Africa's plateau uplift and Cenozoic magmatism (e.g., Huerta et al., 2009; Cornwell et al., 2011; Julià & Nyblade, 2013; Mulibo & Nyblade, 2013a; Thompson et al., 2015; Reed et al., 2016). However, these studies offer limited consensus on the number, geometry and thermochemical nature of upwellings penetrating the East African upper mantle. Several other mid-to-upper mantle low wavespeed anomalies have been interpreted as evidence for mantle upwellings in East Africa (e.g., Chang & Van der Lee, 2011; Chang et al., 2015; Civiero et al., 2015), the Atlas Mountains (e.g., Civiero et al., 2018), Madagascar (e.g., Pratt et al., 2017) and the Cameroon Volcanic Line (e.g., Reusch et al., 2010; French & Romanowicz, 2015; Emry et al., 2019).

2.2 Africa's Archean Cores

The African plate is characterized by numerous Archean cratonic cores that sutured along Paleoproterozoic mobile belts during the ∼550 Ma Pan-African orogeny (e.g., Möller et al., 1998, Figure 1). Deformation and associated subsequent extension is generally localized to the mobile belts (Begg et al., 2009). With the exception of the ≥2.6 Ga Tanzanian craton (Möller et al., 1998), all Africa's Archean domains (e.g., West Africa, Congo, Zimbabwe, Kaapvaal) are underlain by thick lithosphere (≥200 km: Pasyanos & Nyblade, 2007; Fishwick, 2010; Priestley et al., 2019). Surface wave studies reveal seismically fast but unusually thin and asymmetric cratonic lithosphere below Tanzania: ∼175 km thick in the west; ∼135 km thick in the east

(Weeraratne et al., 2003; Adams et al., 2012; O'Donnell et al., 2013; Emry et al., 2019). Intriguingly, the Tanzanian craton hosts an unusually high proportion of Cenozoic kimberlites (Stachel et al., 1998; Tappe et al., 2018, Figure 1). Furthermore, petrological constraints show depleted mantle lithosphere, typical of cratonic cores, exists to only ∼120 km depth beneath Tanzania while the lower lithosphere may have been enriched after formation (Lee & Rudnick, 1999).

2.3 East African Rift Cenozoic Tectonics and Magmatism

Seismically and magmatically active rifting define the topography of East Africa from Ethiopia and Arabia in the north, to southern Africa (Figure 1). The southern Red Sea, Main Ethiopian, and East African Rift systems all developed atop broad topographic plateaus. Uplift of the Ethiopian plateau began 20–30 Ma on the basis of (U-Th)/He geothermometry (Pik et al., 2003), with lithospheric foundering in response to extensive heating of the lithosphere perhaps increasing elevation further in Miocene times (Gani et al., 2007; Furman et al., 2016). East African plateau uplift likely began later, at ∼14 Ma (Wichura et al., 2010). The low-lying Turkana Depression was below sea-level in pre-Neogene times (e.g., Sepulchre et al., 2006), and is thought to have risen by ∼600 m concurrently with East African Plateau uplift. Turkana's complex history of multiple rifting phases allows the possibility that the plateaus are one uplifted region, extending from southern Africa to Ethiopia/Arabia.

Cenozoic magmatism began in southern Ethiopia and Kenya at 45–30 Ma (George et al., 1998; Furman, Bryce, et al., 2006), followed by the emplacement of the 31–29 Ma Ethiopian/Arabian flood basalt province. Subsequent low volume magmatism became pervasive throughout the East African Rift from 10 Ma (e.g., Baker et al., 1996; Rooney, 2020a). There is general consensus in the petrological literature that the Ethiopian and East African mantle is hot (Rooney et al., 2012; Ferguson et al., 2013), with potential temperatures (Tp) elevated by 100–140°C at the present day, following a 170°C peak at 30 Ma.

2.4 Cenozoic Intra-plate Magmatism

Other sites of African Cenozoic magmatic activity exist across the Atlas Mountains, north-central Africa, Madagascar and the Cameroon Volcanic Line (CVL; Figure 1), but their development is less easily attributed to deep mantle plume hypotheses. The CVL, for example, a linear volcanic chain in west Africa, lacks the expected age-progression consistent with traditional plate-plume models (Fitton & Dunlop, 1985). Previous authors have instead suggested shear zone reactivation (e.g., Fairhead, 1988), small-scale convection (e.g., King & Ritsema, 2000; Reusch et al., 2011) and lithospheric delamination (e.g., Milelli et al., 2012; De Plaen et al., 2014) to explain the CVL's protracted, yet sporadic development of small-volume alkali basaltic melts (Suh et al., 2003). Studies attempting to resolve a lower mantle contribution to CVL magmatism have proven inconclusive (e.g., Hansen et al., 2012; French & Romanowicz, 2015; Hosseini et al., 2019). Similarly, although recent tomographic images have revealed slow upper mantle wavespeeds underlying them, Cenozoic magmatic provinces across Madagascar (e.g., Mazzullo et al., 2017; Pratt et al., 2017; Barruol et al., 2019), are not thought to be the result of significant sub-plate thermal anomalies. Instead Madagascan magmatism may result from decompression melting related to uplift, lithospheric thinning and rifting (e.g., Melluso et al., 2016; Cucciniello et al., 2017).

3 Data and Methods

3.1 Global and Regional Data Sets

We use a global data set of P, Pn, Pg, pP, PKP and PKIKP phase absolute arrival-time picks from the "EHB" database (Engdahl et al., 1998) recorded from 1964–2007 (Figure 1; Li et al., 2008). Figures S1–S2 show all earthquakes and stations used in this study. Figure S3 shows mean direct-P absolute arrival-time residuals for Africa and the surrounding regions. The African EHB data set yields 182,853 direct-P phase picks and 48,945 Pn phase picks. Picks from the EHB database are combined with new absolute arrival-time direct-P phase picks from temporary seismograph station deployments from 1994–2019 that greatly improve spatial sampling of the African mantle, particularly in the east and south (red triangles in Figure 1). To glean first-breaking (or onset time) information from these stations for the first-arriving phase, we use AARM, the Absolute Arrival-time Recovery Method (Boyce et al., 2017) to accurately extract 87,184 absolute arrival-times from these temporary seismic deployments. For each earthquake, filtered waveforms (0.4–2.0 Hz) are initially aligned on their first visible coherent peak or trough in a narrow 3 s window following the relative arrival-time approach of VanDecar and Crosson (1990) to determine a set of time shifts. These time shifts are then applied to the original, unfiltered seismograms prior to phase weighted stacking, which is further optimized by weighting each trace in a final stack by its cross-correlation coefficient with the initial stack. The first arrival or onset time exists somewhere prior to the first visible coherent peak or trough that was picked during the relative arrival-time analysis. The separation of first arrival-time and subsequent peak or trough (used previously for phase alignment) is unique to the coherent phase arrival from each teleseismic earthquake across a regional seismic network and is primarily controlled by variable background noise level and coherent phase period. The first arrival is revealed on the high SNR final stack and is picked to extract a common time correction for each earthquake. Absolute arrival-times are extracted by applying the common time correction to the individual trace alignment times. To ensure waveform similarity during the alignment process, the temporary seismic station distribution is split into six subregions, namely; Atlas Mountains, Cameroon, Ethiopia, East African Rift, Madagascar and Southern Africa. Data are processed within these subregions (Figures S4–S16) until being combined in the inversion process below.

AARM-derived mean P-wave absolute arrival-time residuals with respect to ak135 (Kennett et al., 1995) are plotted in Figure 2. Because absolute arrival-time residuals record wavespeed variation encountered along the entire source-to-receiver ray path, the first order variations seen in relative arrival-time studies (e.g., Bastow et al., 2008; Boyce et al., 2016) are not expected. For example, much of southern and eastern Africa displays late mean P-wave absolute arrival-times despite the presence of fast wavespeed cratonic lithosphere. However, the main Ethiopian rift shows the lowest mean absolute arrival-time residuals of $\approx$4 s across Africa and a polarity change from low to high mean arrival-time residuals is observed perpendicular to the CVL - Congo craton boundary (Figure 2).

3.2 Inversion Technique

We employ the tomographic inversion method of Li et al. (2008) and Burdick et al. (2017). Rays are traced through the 1D reference model ak135 and are clustered by station and event location similarity to form composite rays. Composite rays are weighted by the number of constituent rays (Kárason & Van der Hilst, 2001). The initial model is parameterized on a regular, global grid with cells spaced 45 km in depth, 0.35° in latitude and longitude to account for heterogeneity along the entire ray path. In order to account for incomplete global ray path sampling, adjacent under-

sampled grid cells are combined to ensure a minimum of 900 rays per cell (Figure S17). The iterative, linearized, least squares inversion takes place upon the adaptively parameterized grid and is used to solve for hypocenter mislocation and slowness with respect to ak135. This procedure minimizes the following function:

$$\epsilon = \| wGm - wd \|^2 + \lambda_1 \| Lm \|^2 + \lambda_2 \| m \|^2 . \quad (1)$$

In the first term, the ray-theoretical sensitivity matrix, G, model, m, (which includes slowness and hypocenter mislocation parameters) and data, d, are weighted by w. Following previous work, we weight our newly added high-quality absolute arrival-times three times that of the more numerous, yet noisier EHB data set to balance their contribution (e.g., Kárason & Van der Hilst, 2001; Li et al., 2008; Boyce et al., 2019). The inversion is smoothed in the horizontal and vertical directions by the second term, in which L is a first-derivative smoothing operator, and damped by the third (i.e. model norm). These regularization terms are weighted by λ_i relative to the first to control model misfit. λ_i are determined through trade-off analysis (Figure S18) which yields a final model with RMS residual reduction of 49.8% after 400 inversion iterations, although convergence is reached much earlier. We plot P-wavespeed anomalies as a percentage with respect to ak135 and focus on the African portion of the global model-space (40°S – 40°N and 20°W – 60°E).

We account for crustal heterogeneity by making receiver-side corrections to the residuals based on Moho depths within the Crust1.0 model (Laske et al., 2013) supplemented with receiver function constraints for African temporary seismic deployments where available (Akpan et al., 2016; Hosny & Nyblade, 2016; Andriampenomanana et al., 2017; Ebinger et al., 2017; Lemnifi et al., 2017; Fadel et al., 2018; Ogden et al., 2019). Details on generation of this crustal model and its effect on our tomographic inversion are presented in the supplementary material (Figures S19–S21). We propagate rays through the bespoke crustal model, calculate the component of each residual produced by the crustal model and remove this from the data vector (d) prior to the inversion.

3.3 Resolution Assessment

Structural and checkerboard tests (Figures 3, 4, S22–S37) appraise the resolving power of our tomographic model (AFRP20) beneath Africa. Using identical ray paths to the observed data, we calculate arrival-time residuals through synthetic wavespeed models. We invert these data following addition of 0.2 s standard deviation Gaussian noise. Visual defects within input anomaly models arise from imposing our input wavespeed anomalies onto the coarse adaptive grid in poorly sampled regions.

Amplitude recovery of the broad, inclined slow wavespeed structure is ≥60% throughout the mid-to-lower mantle (Figure 3) but is laterally smeared at ≥1000 km depth where grid cells are coarsely spaced (Figure 3). Slow wavespeed amplitude recovery to the northeast of the Tanzanian craton is muted in the upper mantle likely due to limited overlying station coverage and the $\delta V_P = 0\%$ buffer region that surrounds the Tanzanian craton input anomaly. The sub-vertical slow wavespeed anomaly beneath Ethiopia/Afar is recovered at ≥80 % to ≥1200 km depth. Below, amplitude recovery is reduced to ∼30% (Figure 3) with some lateral smearing. A synthetic upper mantle CVL anomaly is smeared vertically to ∼660 km depth with <50% amplitude (Figure S22). Slow mid-mantle wavespeeds associated with the synthetic African Superplume structure to the east are not smeared laterally to below the CVL in our tests (Figure S22). We expect to identify a discontinuity within slow wavespeed anomalies if amplitudes are reduced to <40% of the over-or-underlying anomaly (Figures S23–S24).

Further, we expect to identify a ponded slow wavespeed layer at the base of the MTZ with thickness >45 km (Figure S25).

At broad scales, the west African and Congo cratons are poorly resolved reflecting sparse station density (Figure 3b). Southern African cratons are recovered with ≥60% amplitude but are vertically smeared to ∼140% of input anomaly thickness. The Tanzanian craton is reasonably well recovered laterally, although the surrounding slow wavespeeds do smear inwards towards Tanzania. The uniform thickness (180 km) Tanzanian input anomaly is recovered with ∼70–95% of the input thickness. Amplitude recovery is ∼25% for ≥100 km depths, but is ∼50% at shallower depths (Figure 3b,f).

In the shallow mantle (<300 km) below densely instrumented regions, amplitude recovery of small 2–3° checkerboard anomalies is ∼50–75% (Figures S27–S28) and sharp lateral boundaries of larger 5–10° anomalies are well recovered (Figures S29–S31). Particularly at ∼500–1000 km depth below dense station coverage, larger anomalies are well recovered laterally and exhibit reasonable resolvability in depth. At ≤660 km depth we estimate that ∼300 km length-scale anomalies have ∼50% amplitude recovery beneath eastern and southern Africa. At ≥800 km anomalies are recovered at ∼50% amplitude on lateral length-scales of 750–950 km.

Asymmetrical fast cratonic wavespeeds and underlying slow asthenospheric wavespeeds are reasonably well recovered below the Tanzanian craton (Figure 4). Fast wavespeed amplitude recovery in shallow mantle below the western craton is ∼75% decreasing significantly below ∼90 km depth and to the east. The thicker western region is recovered with ≥80% of the input thickness (Figure 4e), while the thinner eastern region is recovered at approximately the input thickness (Figure 4h). We can therefore be reasonably confident of the depth extent of imaged fast wavespeeds below Tanzania on the length-scale of our vertical parameterization (45 km). The asymmetry of slow wavespeeds underlying Tanzania is reasonably well recovered with peak amplitude recovery of ∼50%, although some lateral smearing does exist. The upper boundary of slow wavespeed anomalies is constrained to within ±100–150 km depth but the lower boundary is poorly constrained due to significant vertical smearing.

A simple rectangular or elliptical fast wavespeed Tanzanian craton is also resolvable (∼50% amplitude, Figures S32–S34). While lateral smearing is relatively minor, inherent vertical smearing is approximately double the anomaly input thickness in the case of no underlying slow wavespeeds (Figure S32–S33). Conversely, when underlain by slow wavespeeds, the depth extent of the fast wavespeed anomaly is recovered at ∼80–100% of the input anomaly thickness but amplitude recovery is reduced to ∼30% (Figure S34). Madagascan resolution tests indicate that although upwards and downward vertical smearing is present (±100 km), if slow wavespeed anomalies are isolated to the upper mantle, wavespeed anomaly amplitudes will decrease rapidly below 660 km depth (Figure S35). Resolution tests of East African upper mantle slow wavespeed anomalies (Figures S36–S37), indicate that if ambient mantle is present below the Turkana Depression, wavespeed anomalies will be significantly muted compared to adjacent slow wavespeed regions, despite the lack of overlying stations.

4 Results

By utilizing AARM (Boyce et al., 2017) to capitalize on African temporary seismograph network data, the AFRP20 tomographic model (Figures 5–9) can resolve short wavelength anomalies in the upper mantle, particularly below densely-instrumented eastern and southern Africa, and larger structures within the mid-to-lower mantle (Figures S22–S37). This method facilitates significant improvement over relative arrival-time tomographic models that lack resolving power below ∼600–800 km

depth (e.g., Bastow et al., 2008; Mulibo & Nyblade, 2013b; Civiero et al., 2015), previous African continental P-wave models (e.g., Hansen et al., 2012) and global P-wave tomographic models (e.g., Montelli et al., 2006; Li et al., 2008; Simmons et al., 2012; Hosseini et al., 2019) less focused on upper mantle resolution (see Figure S38 for comparison with global P-wave models). Lower mantle ray path sampling of our continental data set (Figure S39) indicates that slow wavespeed anomalies can be resolved beneath the Indian Ocean by significant crossing ray coverage. Over-sampling bias is accounted for during the ray clustering procedure.

Above 300 km depth, the upper mantle within AFRP20 is dominated by slow wavespeeds ($\delta V_P \leq$–2%) in the northeast and the fast wavespeed ($\delta V_P \geq$1%) cores of the Zimbabwe and Kaapvaal cratons in the south as well as some parts of the poorly resolved West African and Congo cratons (Figures 5, 8, 9). The fast wavespeed cores beneath Congo and West Africa (e.g., Pasyanos & Nyblade, 2007; Priestley et al., 2008; Begg et al., 2009; Fishwick, 2010) are smeared to ≥410 km depth due to the lack of station coverage (Figures 6, 8). In the mid-to-lower mantle, fast wavespeed anomalies are limited to below western, northeastern and the very southern tip of Africa, likely reflecting the paucity of subduction below the continent since ∼550 Ma. Instead, the mid-to-lower mantle in AFRP20 is dominated by slow wavespeed anomalies and is reflected in the mean absolute delay time of 1.36 s (Figure 2) and average wavespeed anomaly within AFRP20 of $\delta\bar{V}_P$=–0.216% with respect to ak135. In the following sections we highlight key features of AFRP20 in each region where seismograph stations are present and offer comparisons to previous studies.

4.1 East Africa

4.1.1 Upper Mantle

The upper mantle beneath the Main Ethiopian Rift and Ethiopian flood basalt province exhibits the slowest wavespeeds in AFRP20 ($\delta V_P \leq$–4%: Figures 5, 9); wavespeed anomalies beneath the adjacent Afar region are weaker (Figure 9). Slow wavespeeds ($\delta V_P \approx$–2%) also underlie the Arabian flood basalts. Both slow wavespeed anomalies extend below 300 km depth in AFRP20. Although AFRP20 does not include data from seismograph stations in the Turkana Depression of southern Ethiopia and northern Kenya, the slow wavespeed anomalies in the upper mantle ($\delta V_P \approx$–1.25%) are not likely an inversion artifact (Figures S36–S37).

East Africa shows a striking difference in the very shallow mantle compared to the rest of the upper mantle (Figures 4, 5). Fast wavespeeds ($\delta V_P \approx$0.75–1.5%) are generally limited to the upper ∼135 km below the western Tanzanian craton and the upper ∼90 km below the eastern craton (Figures 4, 5). Adjacent isolated slow wavespeed anomalies coincide with resolvable portions of the east and west rift branches at these shallow depths. Below, fast wavespeeds are confined to a small, isolated region beneath western Lake Victoria, while the rest of the Tanzanian mantle, extending beyond 200 km depth only displays slow wavespeeds ($\delta V_P \approx$–0.9%). Although less well resolved (Figures 3, 4), fast wavespeeds are broadly restricted to beneath the adjacent Congo and southern African cratons below the very shallow mantle.

Depending on the imposed underlying slow wavespeed structure, resolution tests (Figures 3, 4, S34) indicate that AFRP20 can resolve depth variability in fast wavespeeds below the Tanzanian craton to within 80–100% of input anomaly thickness on the vertical length-scale of our depth parameterization (45 km). These tests show that thinner input wavespeed anomalies (∼90 km) are recovered with greater reliability in depth than thicker input anomalies (≥180 km), due to the large Pn data set (>1000 arrivals) at East African EHB stations. Surface wave models (e.g., Weeraratne et al., 2003; Adams et al., 2012; O'Donnell et al., 2013; Emry et al., 2019) image asymmetrical fast wavespeeds below Tanzania extending to ∼175 km in the west but are perhaps ∼30–

50 km shallower in the east. While our results also suggest that fast wavespeeds below the Tanzanian craton are thinner than observed for other cratons elsewhere (typically greater than 200 km), our fast P-wavespeeds appear to be thinner still (∼135–90 km) than the fast shear wavespeeds imaged previously.

4.1.2 Mid-to-Lower Mantle

Slow wavespeeds ($\delta V_P \leq$–1%) characterize the mantle transition zone beneath northeast Africa (Figures 6, 8). The slow wavespeed region separates into two distinct anomalies of $\delta V_P \leq$–0.8% below 660 km depth, centered beneath the Ethiopian and Kenyan plateaus (A: ∼8°N, 42°E and B: ∼7°S, 34°E, respectively). Between these slow wavespeed regions, below the Turkana depression, a positive, low amplitude wavespeed anomaly at 900–1200 km depth is also imaged (Figures 6, 8, anomaly C). Two distinct wavespeed anomalies below the uplifted Ethiopian and Kenyan plateaus have been imaged to ∼800 km depth previously in global tomographic models (Montelli et al., 2006; Li et al., 2008; Ritsema et al., 2011; Chang et al., 2015), but their extension into the lower mantle is unclear. Slow wavespeed anomalies penetrating the lower mantle beneath the EAR and/or Arabia have also been imaged by regional studies (e.g., Bastow et al., 2008; Chang & Van der Lee, 2011; Mulibo & Nyblade, 2013b; Civiero et al., 2015), however such studies typically suffer a significant resolution decrease below the upper mantle.

Over the depth range 1300–2300 km, the two slow wavespeed anomalies ($\delta V_P \leq$–0.6%) broaden and separate with depth. The northern anomaly (A), shifts approximately eastwards with depth (Figures 7, 8) and appears to bifurcate at ∼1600 km, reaching the lower mantle below the Indian Ocean, northeast of Madagascar (Figures 5–8). Hosseini et al. (2019) show evidence for distinct slow wavespeeds in the upper and lower mantle below Ethiopia and the Indian Ocean respectively but do not establish a connection between these depths. The southern anomaly (B), often referred to as the African Superplume, extends southwest with increasing depth over a broader spatial footprint (Figures 7, 8) and has been imaged frequently (e.g., Ritsema et al., 1999; Li et al., 2008; Ritsema et al., 2011; Hansen et al., 2012; Chang et al., 2015; Hosseini et al., 2019). Because these anomalies appear to dip out of plane the reader is encouraged to study the cross-sections presented in Figure 8 and the 3D rendering of the AFRP20 tomographic model within the supplementary material (Figures S40–S43). Resolution tests indicate two relatively broad subvertical features are well resolved in the mid-to-lower mantle (Figure 3) and horizontal gaps in these slow wavespeed anomalies would be resolved if present (Figures S23–S24).

4.2 Southern Africa

Southern Africa is dominated by two fast wavespeed regions centered on ∼26°S, 28°E and ∼17°S, 30°E of $\delta V_P \leq$2% (Figures 5, 9). These anomalies are collocated with the Archean Kaapvaal and Zimbabwe cratons (e.g., Begg et al., 2009), in general agreement with previous P-wavespeed results (e.g., Fouch et al., 2004; Youssof et al., 2015). The lateral extent of these fast wavespeed regions narrows significantly between 100–200 km depth (Figure 5). They are separated and surrounded by less anomalous wavespeed domains of $\delta V_P \approx$1%, such as the Proterozoic Limpopo belt. Southwestern Africa hosts a weak but distinct slow wavespeed anomaly ($\delta V_P \approx$–0.3%) at ∼32°S, 21°E, beneath the Namaqua-Natal mobile belt. Similar to the resolution tests, fast wavespeed anomalies in southern Africa are somewhat smeared below 300 km depth (Figure 3, 6) but their amplitudes are greatly reduced ($\delta V_P \leq$0.6%).

4.3 Madagascar

Madagascar's upper mantle is largely characterized by slow wavespeeds of up to $\delta V_P \approx$–0.8%, primarily underlying northern and central Cenozoic magmatic provinces and the southwestern region (Figures 5, 9). Adjacent to the central Madagascan volcanic province, a circular fast wavespeed anomaly exists ($\delta V_P \geq$1.5%), centered at ∼19°S, 48°E. This feature extends to the northeast with depth and is located beneath thicker lithosphere (∼120 km) than is present below adjacent magmatic provinces (Rajaonarison et al., 2020). Resolution tests (Figure S35) demonstrate that this feature is not likely an inversion artifact, although anomaly amplitude appears to be strongly influenced by the crustal correction (Figure S21). Resolution tests also indicate that the extension of slow wavespeeds beneath central Madagascar to below upper mantle depths is not entirely the result of vertical smearing (Figure S35). Regions of slow upper mantle wavespeeds below central and northern Madagascan magmatic provinces have been imaged previously in the depth range ∼80–165 km (Mazzullo et al., 2017; Pratt et al., 2017; Barruol et al., 2019; Emry et al., 2019; Celli et al., 2020). Perhaps due to decreased surface wave resolution beyond the upper mantle, these studies debate whether slow upper mantle wavespeeds extend pervasively to the northeast (e.g., Mazzullo et al., 2017; Barruol et al., 2019) or directly below central Madagascar with depth (e.g., Pratt et al., 2017; Emry et al., 2019). The distinctly slow upper mantle wavespeeds below Madagascar in AFRP20 ($\delta V_P \leq$–0.6%) extend southwest through the mantle transition zone but terminate at ∼1000 km depth (Figure 6).

4.4 Cameroon

The onshore component of the CVL is underlain at 100 km depth by a slow wavespeed anomaly ($\delta V_P \leq$1%: Figures 5, 9) around 7°N, 11°E that extends to the northeast as imaged previously (Reusch et al., 2010; Adams et al., 2015; Emry et al., 2019; Celli et al., 2020). An offshore wavespeed anomaly would not be resolved since station coverage there is limited. To the southeast a fast wavespeed anomaly ($\delta V_P \geq$2%) underlies the Congo Craton. Previous studies (Reusch et al., 2010, 2011; Adams et al., 2015) have suggested that both the slow and adjacent fast wavespeeds beneath the CVL and Congo Craton respectively are limited to the upper 300 km. We observe slow wavespeeds extending below 660 km depth (Figures 5, 6), likely resulting from significant vertical smearing (Figure S22). However, resolution tests indicate that the imaged slow wavespeed connection at mid-mantle depths extending from below the CVL to the lower mantle below southern/eastern Africa is not entirely attributable to further lateral/vertical smearing (Figure S22).

4.5 Atlas Mountains

Below the western Atlas Mountains around 31°N, 7°W, a circular slow wavespeed anomaly ($\delta V_P \approx$–1%) extends from 100–400 km depth (Figures 5, 9), previously associated with lithospheric delamination below the mountain belt (Bezada et al., 2014) or a deep mantle upwelling (Civiero et al., 2018). Beneath the western Alboran Sea at ∼36°N, 4°W, sandwiched between northern Africa and southern Spain, a fast wavespeed anomaly ($\delta V_P \approx$0.75%) at 100 km depth extends to the northeast with increasing depth (Figures 5, 9). This feature is likely associated with the subducted Alboran slab (e.g., Bezada et al., 2014).

5 Discussion

By embedding ≥87,000 high quality P-wave teleseismic absolute arrival-times from seismograph stations across Africa within a global P-wave arrival-time data base and tomographic inversion, AFRP20 offers fresh scope to investigate the African man-

tle across the entire depth range. We begin with an investigation into broad-scale mantle heterogeneity below Africa, before focusing in on upper mantle wavespeed structure below regions of Cenozoic magmatism and cratonic lithosphere that possess good seismograph station coverage (Figures 1, 2).

5.1 Broad-scale African Mantle Structure: Evidence for Multiple Whole-Mantle Upwellings?

AFRP20 illuminates two distinct, diverging, slow wavespeed anomalies in the mid-to-lower mantle (anomalies A and B: Figures 6–8) and so motivates discussion of competing models of plume related magmatism in East Africa. High $^3He/^4He$ ratios (R/Ra≈20) in the Ethiopia-Afar volcanic province and the lack of a depleted MORB mantle source of pre-rift magmas provide compelling support for a deep mantle source for East African Cenozoic magmatism (e.g., Marty et al., 1996; Pik et al., 2006; Nelson et al., 2012). Geochemical measurements and geodynamic models have frequently been interpreted in light of global seismic tomographic models that possess modest African resolution reflecting limited data availability. In a recent review, Rooney (2017) summarized the three most popular mantle plume models invoked to explain East African magmatism: (1) a single thermochemical upwelling feeding all magmatism (e.g., Ebinger & Sleep, 1998; Simmons et al., 2007; Forte et al., 2010; Hansen et al., 2012), (2) two branches of the same thermochemical upwelling feeding northern and southern rift volcanism (e.g., Furman, Kaleta, et al., 2006; Nelson et al., 2012) or (3) two distinct thermochemical upwellings below the northern and southern regions, perhaps sourced at different depths or disparate locations at the core-mantle boundary (e.g., George et al., 1998; Rogers et al., 2000, 2010).

A single thermochemical upwelling feeding East African magmatism was championed by modeling work (Ebinger & Sleep, 1998; Forte et al., 2010) and previous large-scale tomographic models (e.g., Ritsema et al., 1999; Hansen et al., 2012). These studies revealed a broad (>500 km wide) inclined slow wavespeed anomaly extending from the African LLVP in the lower mantle below southern Africa (e.g., Cottaar & Lekić, 2016) to the upper mantle below the EAR in Kenya: the African Superplume. The Superplume in the lower mantle is routinely interpreted to be chemically distinct from 'normal' thermal plume material on account of its inclination (Simmons et al., 2007) and sharp sides (Ni et al., 2002). Apparent plume inclination may result from whole-mantle convection processes (Steinberger & Torsvik, 2012) or the tomographic manifestation of vertically rising plumes at sequentially advanced stages of ascent (Davaille et al., 2005).

A developing body of geochemical literature, documenting variability in isotopic ratios of along-rift magmas but with no clear north-south trend, proposes that erupted basalts are heterogeneous samples of one broad thermochemical upwelling (e.g., Furman, Kaleta, et al., 2006; Nelson et al., 2012; Halldórsson et al., 2014). In this scenario, multiple upper mantle plume stems rise from a common, deep mantle source, the most likely candidate being the African LLVP and overlying Superplume. Heterogeneity may arise from variability in thermochemical entrainment within upper mantle plume branches, lithospheric contamination and geochemical sampling strategies (e.g., Furman, Bryce, et al., 2006; Barry et al., 2013; Williams et al., 2015). Below the Ethiopian and Kenyan plateaus, two narrow cylindrical slow wavespeed anomalies, confined to the upper mantle, underlain by the Superplume structure have been imaged previously (Ritsema et al., 2011; Chang et al., 2015) providing tomographic support for the multiple upper mantle plume stem model. However, these tomographic models utilize fewer African seismic stations than AFRP20. Regional seismic studies have also interpreted a number of small slow wavespeed conduits beneath the EAR and/or Arabia but have lacked resolution into the lower mantle (Chang & Van der Lee, 2011; Civiero et al., 2015; Emry et al., 2019).

Lastly, two distinct thermochemical upwellings below the northern and southern regions, perhaps sourced at different depths or from different regions at the core-mantle boundary are supported by dating (George et al., 1998) and isotopic ratios (Rogers et al., 2000, 2010) of Kenyan and Afar basalts. Geodynamic modeling of African mantle plumes shows that the timings of volcanism are hard to reconcile with a single plume model (Lin et al., 2005), and different plume types/morphologies can coexist in relative proximity (Farnetani & Samuel, 2005).

AFRP20 shows evidence for two slow wavespeed anomalies that extend throughout the mid-to-lower mantle (anomalies A and B: Figures 6–8). Although not readily distinguished in the upper mantle, these anomalies do not appear to merge at greater depth or sample a similar portion of the lower mantle (Figures 3, S23–S25). The elongate heterogeneous wavespeed structure within anomaly B is not easily reconciled with the model of multiple vertically rising plumes at sequentially advanced stages of ascent (Davaille et al., 2005) meaning an alternative mechanism to explain plume tilt is favored below Africa (e.g., Farnetani & Samuel, 2005; Simmons et al., 2007; Steinberger & Torsvik, 2012). Further, supported by specific resolution testing (Figure S25), AFRP20 shows little evidence for a ponded layer of slow wavespeed material at lower mantle transition zone depths, above which multiple upper mantle plume stems could emerge. However, we cannot rule out the presence of a ponded slow wavespeed layer of thickness less than our vertical parameterization of 45 km. Our resolution testing shows that a significant horizontal interruption in slow wavespeeds would also be visible if present (Figures S23–S24). While numerous tomographic models image the African Superplume, tentative evidence for a second anomaly exists within previous models but a clear connection from two anomalies within the mid-mantle to the core-mantle boundary (Montelli et al., 2006; Li et al., 2008; Simmons et al., 2012) or between the upper and lower mantle (Hosseini et al., 2019) is not conclusive (Figure S38). AFRP20 may therefore be the first large-scale tomographic model to convincingly image two distinct whole-mantle plumes underlying East African magmatism.

While AFRP20 cannot constrain uniquely the thermochemical state of the imaged mantle upwellings, their location within the lower mantle is notable. The African Superplume (Figures 6–8, anomaly B) appears to be anchored in the lower mantle (>2300 km depth) west of southern Africa at ∼25°S, 2°E. This correlates well with the African LLVP beneath southern Africa and the Atlantic (Cottaar & Lekić, 2016, see Figure 7d). Although anomaly A appears to bifurcate below ∼1600 km depth, its extent into the lower mantle below the Indian Ocean, northeast of Madagascar, places its source outside the canonical African LLVP (Figure 7d). However, recent multi-frequency P-wave tomography that includes Pdiff phases (Hosseini et al., 2019), shows slow P-wavespeeds collocated with the lower mantle extent of anomaly A. An upwelling rooted outside the conventional LLVP implies a potentially different composition from the upwelling sourced from inside the African LLVP.

5.2 Upper Mantle Structure Below Cenozoic Magmatism

5.2.1 The East African Rift

In Ethiopia, the Miocene-Recent East African Rift exposes subaerially the transition from continental rifting to oceanic spreading within a ∼30 Ma old continental flood basalt province (e.g., Chorowicz, 2005; Rooney, 2017). P-wave absolute arrival-times recorded in the Ethiopian rift are generally delayed by >3 s (Figure 2). The largest station-mean delay time (minimum ten arrivals) is 4.7 s at 9°N, 39.1°E, on the western Ethiopian rift flank. Consequently the most anomalous wavespeeds of $\delta V_P \leq$–4% occur below the western rift flank and adjacent plateau (Figures 5, 8, 9). This corroborates earlier studies in Ethiopia that cite observations of markedly low wavespeeds and delayed phase arrival-times as evidence that the Ethiopian mantle is

amongst the slowest worldwide (e.g., Bastow et al., 2005, 2008). Markedly slow shear wavespeeds ($\delta V_S \leq$–11%) have been also observed in the upper 150 km (Gallacher et al., 2016). AFRP20 also confirms that the slowest upper mantle P-wavespeeds exist below the MER and adjacent Ethiopian plateau, not below Afar (Bastow et al., 2008).

Petrologically-determined mantle potential temperatures (Tp) are elevated by ∼140°C in Ethiopia, toward the low end of the temperature range of global hotspots and large igneous provinces (Rooney et al., 2012). The MER is currently extending at ∼6 mm/yr, slower than the adjacent Red Sea rift at ∼15–20 mm/yr (e.g., Vigny et al., 2006; McClusky et al., 2010) and is doing so without significant crustal thinning (e.g., Mackenzie et al., 2005). Therefore, the anomalously slow wavespeeds cannot be easily attributed to the traditional hotspot model of a purely thermal anomaly or decompression melting due to rapid plate thinning above a mantle plume (White & McKenzie, 1989). Instead, melt likely contributes considerably to our observations, both within and below the lithosphere.

Evidence for melt throughout the Ethiopian lithospheric mantle comes from studies of seismic anisotropy (e.g., Kendall et al., 2005; Bastow et al., 2010), while asthenospheric melt is also required to explain the region's depressed surface wave wavespeeds (Bastow et al., 2010; Gallacher et al., 2016). Below depths at which decompression melting of normal mantle peridotite can reasonably be invoked to explain slow wavespeeds, a hypothesis of CO_2-assisted mantle melting can explain anomalously depressed seismic wavespeeds, beyond those readily interpreted thermally (Rooney et al., 2012). Carbonatite volcanism in East Africa, such as is found at Ol Doinyo Lengai, Tanzania (see Figure 9), does not provide direct evidence for anomalous mantle enrichment of CO_2 (Fischer et al., 2009). However, on the strength of xenolith evidence and CO_2 degassing measurements, carbonatite melts and CO_2 enriched fluids are likely to be present throughout the East African mantle (Rudnick et al., 1993; Frezzotti et al., 2010; Muirhead et al., 2020). Uneven CO_2 availability offers an appealing explanation for the apparent internal wavespeed architecture within a thermochemically heterogeneous upper mantle ($\leq$410 km depth: Figures 5, 8, 9) because AFRP20 is less easily reconciled with ponding of deep sourced plume material below the transition zone rising as plumelets into the upper mantle (e.g., Farnetani & Samuel, 2005; Civiero et al., 2015).

Further south in the EAR, in Kenya, where rifting is at a less mature stage than in Ethiopia (Ebinger et al., 2017), arrival-times are less delayed and consequently upper mantle wavespeeds are less depressed than below Ethiopia (Figures 2, 5, 8, 9). However, petrologically-determined Tp estimates do not differ markedly below Ethiopia and Kenya (Rooney et al., 2012). At <100 km depth, the relative paucity of melt below the EAR in Kenya can explain this observation (Rooney, 2020b). At greater depth, reduced CO_2-driven mantle melting and/or other thermochemical effects may better account for discrepant wavespeeds between the Ethiopian and Kenyan upper mantle.

5.2.2 The Confluence of Multiple Upwellings Below the East African Rift

AFRP20 lacks abrupt separation between slow wavespeeds centered below the Ethiopian and Kenyan plateaus in the upper mantle (<660 km depth), yet below, evidence for two distinct whole-mantle upwellings becomes apparent (Figures 5–8). Our thorough resolution testing (specifically Figures S36–S37) strongly indicates that distinct upper mantle slow wavespeed anomalies below the Ethiopian and Kenyan plateaus separated by ambient mantle below Turkana would be evidenced by significant reduction in negative wavespeed amplitudes, contrary to what is observed in AFRP20. Furthermore, separation of slow wavespeed anomalies below the mantle transition zone,

as observed in AFRP20 is also robust. The persistently depressed wavespeeds below East Africa suggest mixing of heterogeneous material may be taking place in the upper mantle. Mixing of heterogeneous upwellings could be influenced by competing, yet largely unconstrained factors including the thermochemical nature of each upwelling, the motion of Africa prior to docking with Eurasia at ∼30 Ma, the surrounding mantle flow field and the variability in the plume impingement time below the African plate.

Primitive helium signatures are likely sourced from within LLVPs in the lower mantle (e.g., Williams et al., 2019), yet are found along the entire continental rift from Afar to southern Tanzania (Hilton et al., 2011; Halldórsson et al., 2014). This implies that material derived from the African LLVP is present throughout the East African upper mantle (Rooney, 2020b). Incomplete or uneven mixing of heterogeneous material from the deep mantle, largely dominated by that transported from the LLVP in the African Superplume, may explain mantle geochemical signatures of magmatism that vary between the Ethiopian and Kenyan rift branches and so do not easily fit within the single thermochemical upwelling model (e.g., Rogers et al., 2000). Additionally, although the Ethiopian rift is more mature and extending faster than the EAR further south (Saria et al., 2014; Ebinger et al., 2017), we cannot preclude the possibility that additional heating provided by a second plume can, at least in part account for the more anomalous upper mantle wavespeeds (Figures 5, 8, 9) and modestly higher Tp estimates (Rooney et al., 2012) below Ethiopia/Afar.

5.2.3 The Turkana Depression: Rifting or Dynamic Topography?

The cause of the two distinct uplifted topographic plateaus in Ethiopia and Kenya (typically over 1000 m elevation), separated by the Turkana Depression (<500 m elevation) is often attributed, at least in part, to the influence of mantle plumes (e.g., Pik et al., 2008). Some global tomographic models show two distinct slow wavespeed anomalies beneath Ethiopia and Kenya in the upper mantle (e.g., Ritsema et al., 2011; Chang et al., 2015). Higher resolution, continental shear-wave models show some parts of the Turkana Depression to be underlain by slow wavespeeds (Emry et al., 2019; Celli et al., 2020). Presently, it is unclear whether these anomalies are coherent throughout the entire upper mantle depth range or represent active upwellings.

On the strength of resolution tests (Figures S36–S37), AFRP20 suggests slow upper mantle wavespeeds exist below the Turkana Depression meaning it remains challenging to explain the relatively subdued topography of Turkana by present-day upper mantle processes alone. Although we resolve two mid-to-lower mantle upwellings below the uplifted plateaus and a low amplitude, fast wavespeed anomaly at 900–1200 km depth below the Turkana depression between them (Figures 6, 8, anomaly C), surface dynamic topography is broadly controlled by thermal anomalies in the upper mantle (Hager et al., 1985). Alternatively, Turkana is host to a failed, NW-trending, Mesozoic rift system (e.g., Chorowicz, 2005), which may explain Turkana's low elevations. If the Turkana lithosphere had not been thinned by a combination of Mesozoic and more recent Cenozoic rifting events, high elevations may have been continuous across the Ethiopian and Kenyan plateaus. Additional constraints on shallow mantle wavespeeds from body waves will be provided by ongoing work in the Turkana depression.

5.2.4 Non-rift Related Magmatism: A Lower Mantle Contribution to the Cameroon Volcanic Line?

Away from the uplifted Ethiopian and Kenyan plateaus, in Madagascar, Cameroon and the Atlas Mountains, mean absolute arrival-times are typically delayed (≈1–2 s: Figure 2). Accordingly, when compared to Ethiopia, these volcanic centers are characterized by less anomalous upper mantle wavespeed anomalies in AFRP20 (typically –2%≤ δV_P ≤–1%: Figures 5, 9). The cause of magmatism along the CVL has long

been debated because the chain lacks the linear age progression expected for a stationary plume underlying a moving plate (e.g., Fitton & Dunlop, 1985). Lavas along the CVL are typically alkaline basaltic in composition (e.g., Suh et al., 2003) which, when reviewed in light of the region's relatively felsic crust (Gallacher & Bastow, 2012), has led some studies to suggest that low melt volume hypotheses for CVL development such as shear zone reactivation or small-scale convection are most appropriate (e.g., Milelli et al., 2012; Gallacher & Bastow, 2012; Fourel et al., 2013; De Plaen et al., 2014). Our observations of only subtly anomalous absolute arrival-time residuals (Figure 2) and modestly slow wavespeeds below Cameroon compared to the markedly delayed arrivals and $\delta V_P \approx$–4% anomalies below Ethiopia, corroborate this view. Numerous regional studies have also concluded that slow wavespeeds below the CVL are confined to the upper mantle (<410 km depth; Reusch et al., 2010, 2011; Adams et al., 2015).

Synthetic resolution tests (Figure S22) show vertical smearing of the CVL slow wavespeed anomaly to ∼660 km depths. Based on our specific tests, the imaged extension of slow wavespeeds below the CVL upper mantle, southwest to greater depth in AFRP20 (Figure S22e,f) is not entirely the result of smearing. Therefore we cannot preclude the possibility that lower mantle material contributes to magmatism somewhere along the CVL. This agrees with some global tomographic models documenting whole mantle plumes (e.g., French & Romanowicz, 2015) and the continental-scale study of Emry et al. (2019), who suggest that the northern CVL may be fed by deeper material whilst the southern CVL is more consistent with a shallower causal mechanism.

5.3 Cratonic Wavespeed Structure

Temperature generally exerts the strongest control on upper mantle wavespeeds (e.g., Goes et al., 2000). However, the iron-depleted, dry nature of Archean mantle lithosphere at ≤250 km depth typically amplifies fast wavespeed anomalies in tomographic models (e.g., Griffin et al., 2003; Jordan, 1988). Although limited station coverage results in poor lateral wavespeed constraints beneath the Congo and West African cratons, wavespeeds in AFRP20 are well resolved below southern and eastern Africa's Archean cores (Figures 3, 4, S27–S34). In southern Africa, the fastest P-wavespeeds are confined to beneath central Kaapvaal but extend from the central Zimbabwe craton northward, beyond the surficial geological boundary ($\delta V_P \geq$1.5%, 100–300 km depth: Figures 5, 9; also see: Ritsema & Van Heijst, 2000; Debayle et al., 2001; Pasyanos & Nyblade, 2007; Fishwick, 2010). Less-fast wavespeeds reside beneath the eastern, western and southern Kaapvaal and the Proterozoic Limpopo belt (e.g., Fouch et al., 2004; Youssof et al., 2015). Neither our P- (Figure 9) or most recent S-wave tomographic images (Fishwick, 2010; Celli et al., 2020) show a clear relationship between strong lateral velocity gradients and kimberlite locations across southern Africa, in conflict with worldwide observations (e.g., Faure et al., 2011) and other previous African studies (e.g., Priestley et al., 2008; Begg et al., 2009).

A striking observation in Figures 4, 5 and 9 is that fast P-wavespeeds below the Tanzanian craton are largely restricted to shallow mantle depths and perhaps display basal topography, extending only to 135–90 km depth west-to-east. Fast shear wavespeeds are also thinner than expected for typical cratonic cores (≥200 km) and are asymmetric (Weeraratne et al., 2003; Adams et al., 2012; O'Donnell et al., 2013; Emry et al., 2019; Celli et al., 2020); thicker on the western side (∼175 km), thinner on the eastern side (∼135 km). Our fast P-wavespeeds are significantly thinner than the imaged fast shear wavespeeds that on average, provide a better match to petrologically defined lithospheric thickness estimates (∼160 km; Lee & Rudnick, 1999).

Thermal erosion by underlying warm asthenospheric material has been proposed to explain the anomalously thin Tanzanian mantle fast shear wavespeeds (e.g., Weeraratne et al., 2003; Celli et al., 2020). While thermal erosion can explain the anomalously thin Tanzanian lithosphere, it cannot account for the discrepancy between our P-wavespeed images and previous shear wavespeed models because lithospheric removal or increased lithospheric temperatures would decrease both δV_P and δV_S (e.g., Goes et al., 2000; Schutt & Lesher, 2006). Excess water or mantle melting at the plate base would also dramatically reduce δV_S and δV_P (Wagner et al., 2008). We therefore likely require a steady-state compositional explanation for the observed decrease in P-wavespeeds in the lower portion of the anomalously thinned Tanzanian lithosphere.

Tanzanian xenoliths show the mantle lithosphere is depleted, particularly above 120 km depth (Lee & Rudnick, 1999), yet V_P sensitivity to lithospheric depletion is low (Schutt & Lesher, 2006). However, from 120–150 km depth, the initially refractory lithosphere may have undergone refertilization (Lee & Rudnick, 1999), primarily involving silica enrichment of olivine by fluids and/or melt, resulting in orthopyroxene formation (e.g., Lee et al., 2011; Gibson et al., 2013), as observed in on-craton xenolith samples (Stachel et al., 1998; Begg et al., 2009). This process may lower V_P by >1% without affecting V_S or density (Wagner et al., 2008; Schutt & Lesher, 2010) and hence provides an appealing mechanism to reconcile the anticorrelation between P- and S-wavespeed anomalies within the thinned Tanzanian cratonic lithosphere. Wölbern et al. (2012) also suggest the observed mid-lithospheric discontinuity beneath the northwest Tanzanian craton may result from the upper limit of fluid or melt infiltration.

Because on-craton kimberlite samples from 47–53 Ma capture evidence for earlier lithospheric orthopyroxene enrichment (Stachel et al., 1998), prior to the onset of flood basalt related magmatism in East Africa (∼31 Ma George et al., 1998; Baker et al., 1996; Rooney, 2020a), P-wavespeed evidence for metasomatic modification of the Tanzanian craton is best explained by a widespread tectonic process, preceding both kimberlite magmatism and younger, perhaps ongoing, rift or plume related mechanisms (Koornneef et al., 2009; Celli et al., 2020). A clear candidate is therefore Proterozoic-age, 'Pan-African' subduction at ∼550 Ma (Möller et al., 1998). Plume and rift related craton modification may instead favor lithospheric thinning (e.g., Weeraratne et al., 2003; Celli et al., 2020) and marginal processes (Koornneef et al., 2009), respectively. By considering both the impact of prior metasomatic modification, lowering V_P only (Figures 4, 5 and 9) and more recent thermal erosion, evidenced by lowering of both V_S (Weeraratne et al., 2003; Adams et al., 2012; O'Donnell et al., 2013; Emry et al., 2019; Celli et al., 2020) and V_P, we can reconcile seismological and petrological evidence pertinent to the evolution of the Tanzanian cratonic lithosphere.

6 Conclusions

AFRP20 is a new P-wave whole-mantle tomographic model for Africa. It combines data from all temporary broadband seismograph deployments from 1994–2019 with an existing global database of absolute arrival-time measurements. The western flank of the main Ethiopian rift exhibits the largest station-mean absolute arrival-times across Africa (≈4.7 s). Consequently, the upper mantle in this region and adjacent plateau hosts the most anomalous slow P-wavespeeds ($\delta V_P \leq$–4%). We resolve the African Superplume as an inclined, heterogeneous, whole-mantle slow wavespeed structure extending from the African LLVP to the upper mantle below the Kenyan plateau. However, we also image a second whole-mantle slow wavespeed anomaly extending upwards from the core-mantle boundary below the Indian Ocean, distal from the African LLVP, to the upper mantle beneath the Ethiopian plateau. Our tomographic images indicate two, disparately sourced whole-mantle plumes may influence magmatism in East Africa. Other sites of African Cenozoic volcanism such as Cameroon and Mada-

gascar, exhibit much lower amplitude upper mantle wavespeed anomalies than below northeast Africa, but may extend beyond upper mantle depths.

Below the Tanzanian craton, fast P-wavespeeds extend to ∼90–135 km depth. This captures the previously observed asymmetry in depth but is even thinner than corresponding surface wavespeed images. While we cannot constrain whether the Tanzanian craton is presently undergoing thermal erosion (Celli et al., 2020), this provides an appealing explanation for the thinner than global average cratonic thickness of fast P- and S-wavespeeds beneath Tanzania. Our observation of even thinner P-wavespeeds compared to shear wavespeed images is explained best in light of petrological evidence for modification of the lower lithosphere via subduction-driven metasomatism during the ∼550 Ma Pan-African orogeny.

Acknowledgments

A digital model file of AFRP20 will be made available through http://ds.iris.edu/ds/products/emc/ or by contacting the corresponding author (email: ab2568@cam.ac.uk). Phase arrivals from the EHB Bulletin are available at http://www.isc.ac.uk/ehbbulletin/. Seismic data was obtained (last accessed 05 June 2019) from IRIS (https://ds.iris.edu/ds/nodes/dmc/), GFZ (http://geofon.gfz-potsdam.de/) and RESIF (http://seismology.resif.fr/) databases and subsequently processed using IRIS products and ObspyDMT (Hosseini & Sigloch, 2017). Temporary seismograph network codes (with FDSN registered DOI numbers) used to improve resolution over permanent global and national networks include: 1C: Velasco and Kaip (2011), 3D: Thomas (2010), 6A: Heit et al. (2010), 7C: Vergne et al. (2014), 8A: Dias and Haberland (2010), AF: Penn State University (2004), NR: Utrecht University (UU Netherlands) (1983), XA: Silver (1997), XB: Wiens and Nyblade (2005), XD: Owens and Nyblade (1994), XI: Nyblade (2000), XK: Gao and Liu (2012), XV: Wysession et al. (2011), XW: Leroy et al. (2009), XZ: Leroy (2003), YA: Ebinger (2012), YB: Vernon and James (1998), YI: Gaherty and Shillington (2010), YQ: Gaherty and Ebinger (2013), YV: Barruol and Sigloch (2012), YY: Keranen (2013), ZE: Ebinger (2007), ZE: Tilmann et al. (2012), ZF: Fontaine et al. (2015), ZK: Gao (2009), ZP: Nyblade (2007), ZS: Deschamps A. et al. (2007). AARM is available as an electronic supplement to Boyce et al. (2017) or by contacting the corresponding author. Figures were plotted using the Generic Mapping Tools (https://www.generic-mapping-tools.org/).

This paper as been greatly improved following insightful discussions with J. Crosby, S. Gibson, K. Priestley, S. Stephenson and T. Rooney. We are grateful for reviewer suggestions that helped to more clearly lay out the themes of our discussion and clarify our description of Tanzanian craton modification. The authors thank E. M. Golos, S. Burdick and R. D. Van der Hilst for use of the global tomographic inversion code. A. B. also thanks M. Maitra and S. Pilia for assistance with resolution tests. A. B. and S. C. are funded by the Natural Environment Research Council (NERC) Grant number NE/R010862/1 from PI Cottaar in Cambridge. A. B. was previously funded by the NERC Doctoral Training Partnership: Science and Solutions for a Changing Planet - Grant number NE/L002515/1 at Imperial College. I. B is funded by Natural Environment Research Council Grant number NE/S014136/1.

References

Adams, A. N., Nyblade, A. A., & Weeraratne, D. (2012). Upper mantle shear wave velocity structure beneath the East African plateau: evidence for a deep, plateauwide low velocity anomaly. *Geophys. J. Int.*, *189*(1), 123–142. doi: 10.1111/j.1365-246x.2012.05373.x

Adams, A. N., Wiens, D. A., Nyblade, A. A., Euler, G. G., Shore, P. J., & Tibi, R.

(2015). Lithospheric instability and the source of the Cameroon Volcanic Line: Evidence from Rayleigh wave phase velocity tomography. *J. Geophys. Res.*, *120*(3), 1708–1727. doi: 10.1002/2014jb011580

Akpan, O., Nyblade, A. A., Okereke, C., Oden, M., Emry, E., & Julià, J. (2016). Crustal structure of Nigeria and Southern Ghana, West Africa from P-wave receiver functions. *Tectonophysics*, *676*, 250–260. doi: 10.1016/j.tecto.2016.02.005

Andriampenomanana, F., Nyblade, A. A., Wysession, M. E., Durrheim, R. J., Tilmann, F., Julià, J., ... Rakotondraibe, T. (2017). The structure of the crust and uppermost mantle beneath Madagascar. *Geophys. J. Int.*, *210*(3), 1525–1544. doi: 10.1093/gji/ggx243

Baker, J., Snee, L., & Menzies, M. (1996). A brief Oligocene period of flood volcanism in Yemen. *Earth Planet. Sci. Lett.*, *138*, 39-55. doi: 10.1016/0012-821x(95)00229-6

Barruol, G., & Sigloch, K. (2012). *RHUM-RUM experiment, 2011-2015, (Réunion Hotspot and Upper Mantle – Réunion's Unterer Mantel).* RESIF - Réseau Sismologique et géodésique Français. (Seismic Network) doi: 10.15778/RESIF.YV2011

Barruol, G., Sigloch, K., Scholz, J. R., Mazzullo, A., Stutzmann, E., Montagner, J. P., ... Dyment, J. (2019). Large-scale flow of Indian Ocean asthenosphere driven by Réunion plume. *Nat. Geosci.*, *12*(12), 1043–1049. doi: 10.1038/s41561-019-0479-3

Barry, P. H., Hilton, D. R., Fischer, T. P., Moor, J. M. d., Mangasini, F., & Ramirez, C. (2013). Helium and carbon isotope systematics of cold "mazuku" CO2 vents and hydrothermal gases and fluids from Rungwe Volcanic Province, southern Tanzania. *Chemical Geology*, *339*, 141–156. doi: 10.1016/j.chemgeo.2012.07.003

Bastow, I. D. (2012). Relative arrival-time upper-mantle tomography and the elusive background mean. *Geophys. J. Int.*, *190*(2), 1271-1278. doi: 10.1111/j.1365-246X.2012.05559.x

Bastow, I. D., Nyblade, A. A., Stuart, G., Rooney, T. O., & Benoit, M. (2008). Upper Mantle Seismic Structure Beneath the Ethiopian Hotspot: Rifting at the Edge of the African Low Velocity Anomaly. *Geochem. Geophys. Geosyst.*, *9*(12). doi: 10.1029/2008GC002107

Bastow, I. D., Pilidou, S., Kendall, J.-M., & Stuart, G. (2010). Melt-induced seismic anisotropy and magma assisted rifting in Ethiopia: evidence from surface waves. *Geochem. Geophys. Geosyst.*, *11*. doi: 10.1029/2010GC003036

Bastow, I. D., Stuart, G., Kendall, J.-M., & Ebinger, C. J. (2005). Upper-mantle seismic structure in a region of incipient continental breakup: northern Ethiopian rift. *Geophys. J. Int.*, *162*(2), 479–493. doi: 10.1111/j.1365-246X.2005.02666.x

Begg, G., Griffin, W., Natapov, L., O'Reilly, S. Y., Grand, S., O'Neill, C., ... Bowden, P. (2009). The lithospheric architecture of Africa: Seismic tomography, mantle petrology, and tectonic evolution. *Geosphere*, *5*(1), 23-50. doi: 10.1130/GES00179.1

Bezada, M. J., Humphreys, E. D., Davila, J., Carbonell, R., Harnafi, M., Palomeras, I., & Levander, A. (2014). Piecewise delamination of Moroccan lithosphere from beneath the Atlas Mountains. *Geochem. Geophys. Geosyst.*, *15*(4), 975–985. doi: 10.1002/2013gc005059

Boyce, A., Bastow, I. D., Darbyshire, F. A., Ellwood, A. G., Gilligan, A., Levin, V., & Menke, W. (2016). Subduction beneath Laurentia modified the eastern North American cratonic edge: Evidence from P wave and S wave tomography. *J. Geophys. Res.*, *121*(7), 5013–5030. doi: 10.1002/2016JB012838

Boyce, A., Bastow, I. D., Golos, E. M., Rondenay, S., Burdick, S., & Van der Hilst, R. D. (2019). Variable modification of continental lithosphere during the

Proterozoic Grenville orogeny: Evidence from teleseismic P-wave tomography. *Earth Planet. Sci. Lett.*, *525*, 115763. doi: 10.1016/j.epsl.2019.115763

Boyce, A., Bastow, I. D., Rondenay, S., & Van der Hilst, R. D. (2017). From relative to absolute teleseismic travel-times: the Absolute Arrival-time Recovery Method (AARM). *Bull. Seis. Soc. Am.*, *107*(5), 2511—2520. doi: 10.1785/0120170021

Burdick, S., Vernon, F. L., Martynov, V., Eakins, J., Cox, T., Tytell, J., ... Van der Hilst, R. D. (2017). Model Update May 2016: Upper-Mantle Heterogeneity beneath North America from Travel-Time Tomography with Global and USArray Data. *Seis. Res. Lett.*, *88*(2A), 319–325. doi: 10.1785/0220160186

Celli, N. L., Lebedev, S., Schaeffer, A. J., & Gaina, C. (2020). African cratonic lithosphere carved by mantle plumes. *Nat. Comms.*, *11*(1), 92. doi: 10.1038/s41467-019-13871-2

Chang, S. J., Ferreira, A. M. G., Ritsema, J., van Heijst, H. J., & Woodhouse, J. H. (2015). Joint inversion for global isotropic and radially anisotropic mantle structure including crustal thickness perturbations. *J. Geophys. Res.*, *120*(6), 4278–4300. doi: 10.1002/2014jb011824

Chang, S. J., & Van der Lee, S. (2011). Mantle plumes and associated flow beneath Arabia and East Africa. *Earth Planet. Sci. Lett.*, *302*(3-4), 448–454. doi: 10.1016/j.epsl.2010.12.050

Chorowicz, J. (2005). The East African rift system. *J. Afr. Earth Sci.*, *43*(1-3), 379–410. doi: 10.1016/j.jafrearsci.2005.07.019

Civiero, C., Hammond, J. O. S., Goes, S., Fishwick, S., Ahmed, A., Ayele, A., ... Stuart, G. W. (2015). Multiple mantle upwellings in the transition zone beneath the northern East-African Rift system from relative P-wave travel-time tomography. *Geochem. Geophys. Geosyst.*, *16*(9), 2949–2968. doi: 10.1002/2015GC005948

Civiero, C., Strak, V., Custódio, S., Silveira, G., Rawlinson, N., Arroucau, P., & Corela, C. (2018). A common deep source for upper-mantle upwellings below the Ibero-western Maghreb region from teleseismic P-wave travel-time tomography. *Earth Planet. Sci. Lett.*, *499*, 157–172. doi: 10.1016/j.epsl.2018.07.024

Cornwell, D., Hetényi, G., & Blanchard, T. (2011). Mantle transition zone variations beneath the Ethiopian Rift and Afar: Chemical heterogeneity within a hot mantle? *Geophys. Res. Lett.*, *38*(16). doi: 10.1029/2011gl047575

Cottaar, S., & Lekić, V. (2016). Morphology of seismically slow lower-mantle structures. *Geophys. J. Int.*, *207*(2), 1122–1136. doi: 10.1093/gji/ggw324

Cucciniello, C., Melluso, L., Roex, A. P. l., Jourdan, F., Morra, V., Gennaro, R. d., & Grifa, C. (2017). From olivine nephelinite, basanite and basalt to peralkaline trachyphonolite and comendite in the Ankaratra volcanic complex, Madagascar: 40Ar/39Ar ages, phase compositions and bulk-rock geochemical and isotopic evolution. *Lithos*, *274*, 363–382. doi: 10.1016/j.lithos.2016.12.026

Davaille, A., Stutzmann, E., Silveira, G., Besse, J., & Courtillot, V. (2005). Convective patterns under the Indo-Atlantic box. *Earth Planet. Sci. Lett.*, *239*(3-4), 233–252. doi: 10.1016/j.epsl.2005.07.024

Debayle, E., Lévêque, J., & Cara, M. (2001). Seismic evidence for a deeply rooted low-velocity anomaly in the upper mantle beneath the northeastern Afro/Arabian continent. *Earth Planet. Sci. Lett.*, *193*(3-4), 423–436. doi: 10.1016/S0012-821X(01)00509-X

De Plaen, R. S. M., Bastow, I. D., Chambers, E. L., Keir, D., Gallacher, R. J., & Keane, J. (2014). The development of magmatism along the Cameroon Volcanic Line: Evidence from seismicity and seismic anisotropy. *J. Geophys. Res.*, *119*(5), 4233–4252. doi: 10.1002/2013jb010583

Deschamps A., Déverchère, J., & Ferdinand, R. (2007). *Seismotanz'07.* RESIF - Réseau Sismologique et géodésique Français. (Seismic Network) doi: 10.15778/RESIF.ZS2007

Dias, G., N. A. Silveira, & Haberland, C. (2010). *Data of the temporary seismic WILAS network.* Deutsches GeoForschungsZentrum GFZ. (Seismic Network) doi: 10.14470/3N7565750319

Ebinger, C. J. (2007). *AFAR.* International Federation of Digital Seismograph Networks. (Seismic Network) doi: 10.7914/SN/ZE_2007

Ebinger, C. J. (2012). *Dynamics of the Lake Kivu System.* International Federation of Digital Seismograph Networks. (Seismic Network) doi: 10.7914/SN/YA_2012

Ebinger, C. J., Keir, D., Bastow, I. D., Whaler, K., Hammond, J. O. S., Ayele, A., ... Hautot, S. (2017). Crustal Structure of Active Deformation Zones in Africa: Implications for Global Crustal Processes. *Tectonics*, *36*(12), 3298–3332. doi: 10.1002/2017tc004526

Ebinger, C. J., & Sleep, N. (1998). Cenozoic magmatism throughout East Africa resulting from impact of a single plume. *Nature*, *395*, 788-791. doi: 10.1038/27417

Emry, E. L., Shen, Y., Nyblade, A. A., Flinders, A., & Bao, X. (2019). Upper Mantle Earth Structure in Africa From Full-Wave Ambient Noise Tomography. *Geochem. Geophys. Geosyst.*. doi: 10.1029/2018gc007804

Engdahl, E. R., Van der Hilst, R. D., & Buland, R. (1998). Global teleseismic earthquake relocation with improved travel times and procedures for depth determination. *Bull. Seis. Soc. Am.*, *88*(3), 722–743.

Fadel, I., Meijde, M., & Paulssen, H. (2018). Crustal Structure and Dynamics of Botswana. *J. Geophys. Res.*, *123*(12), 10,659–10,671. doi: 10.1029/2018jb016190

Fairhead, J. (1988). Mesozoic Plate Tectonic Reconstructions of the Central South Atlantic Ocean: The Role of the West and Central African Rift System. *Tectonophysics*, *155*(1-4), 181–191.

Farnetani, C. G., & Samuel, H. (2005). Beyond the thermal plume paradigm. *Geophys. Res. Lett.*, *32*(7). doi: 10.1029/2005gl022360

Faure, S., Godey, S., Fallara, F., & Trépanier, S. (2011). Seismic Architecture of the Archean North American Mantle and Its Relationship to Diamondiferous Kimberlite Fields. *Economic Geology*, *106*(2), 223–240. doi: 10.2113/econgeo.106.2.223

Ferguson, D., Maclennan, J., Bastow, I. D., Pyle, D., Jones, S., Keir, D., ... Yirgu, G. (2013). Melting during late-stage rifting in Afar is hot and deep. *Nature*, *499*(7456), 70–73. doi: 10.1038/nature12292

Fischer, T. P., Burnard, P., Marty, B., Hilton, D. R., Füri, E., Palhol, F., ... Mangasini, F. (2009). Upper-mantle volatile chemistry at Oldoinyo Lengai volcano and the origin of carbonatites. *Nature*, *459*(7243), 77–80. doi: 10.1038/nature07977

Fishwick, S. (2010). Surface Wave Tomography: Imaging of the Lithosphere-Asthenosphere Boundary Beneath Central and Southern Africa? *Lithos*, *120*(1-2), 63–73. doi: 10.1016/j.lithos.2010.05.011

Fitton, J., & Dunlop, H. (1985). The Cameroon Line, West Africa, and its Bearing on the Origin of Oceanic and Continental Alkali Basalt. *Earth Planet. Sci. Lett.*, *72*(1), 23–38. doi: 10.1016/0012-821x(85)90114-1

Fontaine, F. R., Barruol, G., & Gonzalez, A. (2015). *Rivière des Pluies Project, La Réunion Island, 2015-2018.* RESIF - Réseau Sismologique et géodésique Français. (Seismic Network) doi: 10.15778/RESIF.ZF2015

Forte, A. M., Quéré, S., Moucha, R., Simmons, N. A., Grand, S. P., Mitrovica, J. X., & Rowley, D. B. (2010). Joint seismic–geodynamic-mineral physical modelling of African geodynamics: A reconciliation of deep-mantle convection with surface geophysical constraints. *Earth Planet. Sci. Lett.*, *295*(3-4), 329–341. doi: 10.1016/j.epsl.2010.03.017

Fouch, M., James, D., VanDecar, J., & van der Lee, S. (2004). Mantle seismic struc-

ture beneath the Kaapvaal and Zimbabwe Cratons. *S. Afr. J. Geol.*, *107*(1-2), 33–44. doi: 10.2113/107.1-2.33

Fourel, L., Milelli, L., Jaupart, C., & Limare, A. (2013). Generation of continental rifts, basins, and swells by lithosphere instabilities. *J. Geophys. Res.*, *118*, 3080–3100. doi: 10.1002/jgrb.50218

French, S. W., & Romanowicz, B. (2015). Broad plumes rooted at the base of the Earth's mantle beneath major hotspots. *Nature*, *525*(7567), 95–99. doi: 10.1038/nature14876

Frezzotti, M. L., Ferrando, S., Peccerillo, A., Petrelli, M., Tecce, F., & Perucchi, A. (2010). Chlorine-rich metasomatic H2O–CO2 fluids in amphibole-bearing peridotites from Injibara (Lake Tana region, Ethiopian plateau): Nature and evolution of volatiles in the mantle of a region of continental flood basalts. *Geochimica et Cosmochimica Acta*, *74*(10), 3023–3039. doi: 10.1016/j.gca.2010.02.007

Furman, T., Bryce, J. G., Rooney, T. O., Hanan, B. B., Yirgu, G., & Ayalew, D. (2006). Heads and tails: 30 million years of the Afar plume. *Geol. Soc. Lond. Spec. Pub.*, *259*(1), 95–119. doi: 10.1144/GSL.SP.2006.259.01.09

Furman, T., Kaleta, K. M., Bryce, J. G., & Hanan, B. B. (2006). Tertiary Mafic Lavas of Turkana, Kenya: Constraints on East African Plume Structure and the Occurrence of High-μ Volcanism in Africa. *J. Petrol.*, *47*(6), 1221–1244. doi: 10.1093/petrology/egl009

Furman, T., Nelson, W. R., & Elkins-Tanton, L. T. (2016). Evolution of the East African rift: Drip magmatism, lithospheric thinning and mafic volcanism. *Geochimica et Cosmochimica Acta*, *185*, 418–434. doi: 10.1016/j.gca.2016.03.024

Gaherty, J. B., & Ebinger, C. J. (2013). *Study of extension and magmatism in malawi and tanzania.* International Federation of Digital Seismograph Networks. (Seismic Network) doi: 10.7914/SN/YQ_2013

Gaherty, J. B., & Shillington, D. (2010). *2009 Malawi Earthquake RAMP Response.* International Federation of Digital Seismograph Networks. (Seismic Network) doi: 10.7914/SN/YI_2010

Gallacher, R. J., & Bastow, I. D. (2012). The development of Magmatism Along the Cameroon Volcanic Line: Evidence from Teleseismic Receiver Functions. *Tectonics*, *31*. doi: 10.1029/2011TC003028

Gallacher, R. J., Keir, D., Harmon, N., Stuart, G., Leroy, S., Hammond, J. O. S., ... Ahmed, A. (2016). The initiation of segmented buoyancy-driven melting during continental breakup. *Nature Communications*, *7*(1), 13110. doi: 10.1038/ncomms13110

Gani, N. D. S., Gani, M. R., & Abdelsalam, M. G. (2007). Blue Nile incision on the Ethiopian Plateau: Pulsed plateau growth, Pliocene uplift, and hominin evolution. *GSA Today*, *17*(9), 4–11. doi: 10.1130/gsat01709a.1

Gao, S. S. (2009). *Four-Dimensional Anatomy of Continental Rifts Transitioning into Sea Floor spreading: Insights from Afar, Ethiopia for oil and gas exploration of global rift systems and passive continental margins.* International Federation of Digital Seismograph Networks. (Seismic Network) doi: 10.7914/SN/ZK_2009

Gao, S. S., & Liu, K. H. (2012). *Passive seismic study of early rifting in Botswana, Zambia, and Malawi.* International Federation of Digital Seismograph Networks. (Seismic Network) doi: 10.7914/SN/XK_2012

George, R., Rogers, N. W., & Kelley, S. (1998). Earliest magmatism in Ethiopia: evidence for two mantle plumes in one continental flood basalt province. *Geology*, *26*, 923-926. doi: 10.1130/0091-7613(1998)026⟨0923:EMIEEF⟩2.3.CO;2

Gibson, S. A., McMahon, S. C., Day, J. A., & Dawson, J. B. (2013). Highly Refractory Lithospheric Mantle beneath the Tanzanian Craton: Evidence from Lashaine Pre-metasomatic Garnet-bearing Peridotites. *Journal of Petrology*,

54(8), 1503–1546. doi: 10.1093/petrology/egt020

Goes, S., R., G., & Vacher, P. (2000). Shallow mantle temperatures under Europe from P and S wave tomography. *J. Geophys. Res.*, *105*(B5), 111153-11169. doi: 10.1029/1999JB900300

Griffin, W., O'Reilly, S., Abe, N., Aulbach, S., Davies, R., Pearson, N., ... Kivi, K. (2003). The origin and evolution of Archean lithospheric mantle. *Precamb. Res.*, *127*(1-3), 19–41. doi: 10.1016/S0301-9268(03)00180-3

Hager, B. H., Clayton, R. W., Richards, M. A., Comer, R. P., & Dziewonski, A. M. (1985). Lower mantle heterogeneity, dynamic topography and the geoid. *Nature*, *313*(6003), 541–545. doi: 10.1038/313541a0

Halldórsson, S. A., Hilton, D. R., Scarsi, P., Abebe, T., & Hopp, J. (2014). A common mantle plume source beneath the entire East African Rift System revealed by coupled helium-neon systematics. *Geophys. Res. Lett.*, *41*(7), 2304–2311. doi: 10.1002/2014gl059424

Hansen, S. E., & Nyblade, A. A. (2013). The deep seismic structure of the Ethiopia/Afar hotspot and the African superplume. *Geophys. J. Int.*, *194*(1), 118–124. doi: 10.1093/gji/ggt116

Hansen, S. E., Nyblade, A. A., & Benoit, M. H. (2012). Mantle structure beneath Africa and Arabia from adaptively parameterized P-wave tomography: Implications for the origin of Cenozoic Afro-Arabian tectonism. *Earth Planet. Sci. Lett.*, *319*, 23–34. doi: 10.1016/j.epsl.2011.12.023

Heit, B., Yuan, X., Jokat, W., Weber, M., & Geissler, W. (2010). *WALPASS Network, Namibia, 2010/2012.* Deutsches GeoForschungsZentrum GFZ. (Seismic Network) doi: 10.14470/1N134371

Hilton, D. R., Halldórsson, S. A., Barry, P. H., Fischer, T. P., Moor, J. M. d., Ramirez, C. J., ... Scarsi, P. (2011). Helium isotopes at Rungwe Volcanic Province, Tanzania, and the origin of East African Plateaux. *Geophys. Res. Lett.*, *38*(21). doi: 10.1029/2011gl049589

Hosny, A., & Nyblade, A. A. (2016). The crustal structure of Egypt and the northern Red Sea region. *Tectonophysics*, *687*, 257–267. doi: 10.1016/j.tecto.2016.06.003

Hosseini, K., & Sigloch, K. (2017). ObspyDMT: a Python toolbox for retrieving and processing large seismological data sets. *Solid Earth*, *8*(5), 1047–1070. doi: 10.5194/se-8-1047-2017

Hosseini, K., Sigloch, K., Tsekhmistrenko, M., Zaheri, A., Nissen-Meyer, T., & Igel, H. (2019). Global mantle structure from multifrequency tomography using P, PP and P-diffracted waves. *Geophys. J. Int.*, *220*(1), 96–141. doi: 10.1093/gji/ggz394

Huerta, A. D., Nyblade, A. A., & Reusch, A. M. (2009). Mantle transition zone structure beneath Kenya and Tanzania: more evidence for a deep-seated thermal upwelling in the mantle. *Geophys. J. Int.*, *177*(3), 1249–1255. doi: 10.1111/j.1365-246x.2009.04092.x

Jordan, T. (1988). Structure and formation of the continental tectosphere. *J. Petrol.*, *(Special Lithosphere Issue)*(1), 11-37. doi: 10.1093/petrology/Special_Volume.1.11

Julià, J., & Nyblade, A. A. (2013). Probing the upper mantle transition zone under Africa with P520s conversions: Implications for temperature and composition. *Earth Planet. Sci. Lett.*, *368*, 151–162. doi: 10.1016/j.epsl.2013.02.021

Kárason, H., & Van der Hilst, R. D. (2001). Tomographic imaging of the lowermost mantle with differential times of refracted and diffracted core phases (PKP , P diff). *J. Geophys. Res.*, *106*(B4), 6569–6587. doi: 10.1029/2000jb900380

Kendall, J.-M., Stuart, G., Ebinger, C. J., Bastow, I. D., & Keir, D. (2005). Magma assisted rifting in Ethiopia. *Nature*, *433*, 146-148. doi: 10.1038/nature03161

Kennett, B. L. N., Engdahl, E. R., & Buland, R. (1995). Constraints on seismic velocities in the earth from traveltimes. *Geophys. J. Int.*, *122*(1), 108-124. doi:

10.1111/j.1365-246X.1995.tb03540.x

Keranen, K. (2013). *Exploring extensional tectonics beyond the ethiopian rift.* International Federation of Digital Seismograph Networks. (Seismic Network) doi: 10.7914/SN/YY_2013

King, S. D., & Ritsema, J. (2000). African Hot Spot Volcanism: Small-Scale Convection in the Upper Mantle Beneath Cratons. *Science*, *290*(5494), 1137–1140. doi: 10.1126/science.290.5494.1137

Koornneef, J. M., Davies, G. R., Döpp, S. P., Vukmanovic, Z., Nikogosian, I. K., & Mason, P. R. D. (2009). Nature and timing of multiple metasomatic events in the sub-cratonic lithosphere beneath Labait, Tanzania. *Lithos*, *112*, 896–912. doi: 10.1016/j.lithos.2009.04.039

Laske, G., Masters., G., Ma, Z., & Pasyanos, M. E. (2013). Update on CRUST1.0 - A 1-degree Global Model of Earth's Crust. In *Geophys. res. abstracts, 15, abstract egu2013-2658* (p. EGU2013-2658).

Lee, C. T. A., Luffi, P., & Chin, E. J. (2011). Building and destroying continental mantle. *Ann. Rev. Earth Planet. Sci.*, *39*, 59–90. doi: 10.1146/annurev-earth-040610-133505

Lee, C. T. A., & Rudnick, R. L. (1999). Compositionally stratified cratonic lithosphere: petrology and geochemistry of peridotite xenoliths from the Labait tuff cone, Tanzania. In J. Gurney, J. Gurney, M. Pascoe, & S. Richardson (Eds.), *Proc. 7th int. kimberl. conf.* (Vol. J.B. Dawson Vol., pp. 503—521). Cape Town, S. Afr.

Lemnifi, A. A., Elshaafi, A., Browning, J., Aouad, N. S., El Ebaidi, S. K., Liu, K. K., & Gudmundsson, A. (2017). Crustal Thickness Beneath Libya and the Origin of Partial Melt Beneath AS Sawda Volcanic Province From Receiver Function Constraints. *J. Geophys. Res.*, *122*(12), 10,037–10,051. doi: 10.1002/2017jb014291

Leroy, S. (2003). *DHOFAR Seismic Experiment.* International Federation of Digital Seismograph Networks. (Seismic Network) doi: 10.7914/SN/XZ_2003

Leroy, S., Keir, D., & Stuart, G. W. (2009). *Young Conjugate Margins Lab in the Gulf of Aden.* International Federation of Digital Seismograph Networks. (Seismic Network) doi: 10.7914/SN/XW_2009

Li, C., Van der Hilst, R. D., Engdahl, R., & Burdick, S. (2008). A new global model for P wave speed variations in Earth's mantle. *Geochem. Geophys. Geosyst.*, *9*(5). doi: 10.1029/2007GC001806

Liao, J., Wang, Q., Gerya, T., & Ballmer, M. D. (2017, 9). Modeling Craton Destruction by Hydration-Induced Weakening of the Upper Mantle. *J. Geophys. Res.*, *122*(9), 7449–7466. doi: 10.1002/2017JB014157

Lin, S.-C., Kuo, B.-Y., Chiao, L.-Y., & van Keken, P. E. (2005). Thermal plume models and melt generation in East Africa: A dynamic modeling approach. *Earth Planet. Sci. Lett.*, *237*(1-2), 175–192. doi: 10.1016/j.epsl.2005.04.049

Mackenzie, G., Thybo, H., & Maguire, P. K. H. (2005). Crustal velocity structure across the Main Ethiopian Rift: Results from 2-dimensional wide-angle seismic modelling. *Geophys. J. Int.*, *162*, 994-1006. doi: 10.1111/j.1365-246X.2005.02710.x

Marty, B., Pik, R., & Yirgu, G. (1996). Helium isotopic variations in Ethiopian plume lavas: nature of magmatic sources and limit on lower mantle contribution. *Earth Planet. Sci. Lett.*, *144*(1-2), 223–237. doi: 10.1016/0012-821x(96)00158-6

Mazzullo, A., Stutzmann, E., Montagner, J. P., Kiselev, S., Maurya, S., Barruol, G., & Sigloch, K. (2017). Anisotropic Tomography Around La Réunion Island From Rayleigh Waves. *J. Geophys. Res.*, *122*(11), 9132–9148. doi: 10.1002/2017jb014354

McClusky, S., Reilinger, R., Ogubazghi, G., Amleson, A., Healeb, B., Vernant, P., ... Kogan, L. (2010). Kinematics of the southern Red Sea-Afar Triple Junc-

tion and implications for plate dynamics. *Geophys. Res. Lett.*, *37*(5). doi: 10.1029/2009gl041127

Melluso, L., Cucciniello, C., Roex, A. l., & Morra, V. (2016). The geochemistry of primitive volcanic rocks of the Ankaratra volcanic complex, and source enrichment processes in the genesis of the Cenozoic magmatism in Madagascar. *Geochimica et Cosmochimica Acta*, *185*, 435–452. doi: 10.1016/j.gca.2016.04.005

Milelli, L., Fourel, L., & Jaupart, C. (2012). A lithospheric instability origin for the Cameroon Volcanic Line. *Earth Planet. Sci. Lett.*, *335-336*, 80-87. doi: 10 .1016/j.epsl.2012.04.028

Möller, A., Mezger, K., & Schenk, V. (1998). Crustal Age Domains and the Evolution of the Continental Crust in the Mozambique Belt of Tanzania: Combined Sm-Nd, Rb-Sr, and Pb-Pb Isotopic Evidence. *J. Petrol.*, *39*(4), 749–783. doi: 10.1093/petroj/39.4.749

Montelli, R., Nolet, G., Dahlen, F., & Masters, G. (2006). A catalogue of deep mantle plumes: new results from finite-frequency tomography. *Geochem. Geophys. Geosyst.*, *7*, Q11007. doi: 10.1029/2006GC001248

Muirhead, J. D., Fischer, T. P., Oliva, S. J., Laizer, A., van Wijk, J., Currie, C. A., ... Ebinger, C. J. (2020). Displaced cratonic mantle concentrates deep carbon during continental rifting. *Nature*, *582*(7810), 67–72. doi: 10.1038/s41586-020-2328-3

Mulibo, G. D., & Nyblade, A. A. (2013a). Mantle transition zone thinning beneath eastern Africa: Evidence for a whole-mantle superplume structure. *Geophys. Res. Lett.*, *40*(14), 3562–3566. doi: 10.1002/grl.50694

Mulibo, G. D., & Nyblade, A. A. (2013b). The P and S wave velocity structure of the mantle beneath eastern Africa and the African superplume anomaly. *Geochem. Geophys. Geosyst.*, *14*(8), 2696–2715. doi: 10.1002/ggge.20150

Nelson, W. R., Furman, T., van Keken, P. E., Shirey, S. B., & Hanan, B. B. (2012). OsHf isotopic insight into mantle plume dynamics beneath the East African Rift System. *Chemical Geology*, *320*(189), 66–79. doi: 10.1016/j.chemgeo.2012.05.020

Ni, S., Tan, E., Gurnis, M., & Helmberger, D. (2002). Sharp Sides to the African Superplume. *Science*, *296*(5574), 1850-1852. doi: 10.1126/science.1070698

Nyblade, A. A. (2000). *Seismic Investigation of Deep Structure Beneath the Ethiopian Plateau and Afar Depression.* International Federation of Digital Seismograph Networks. (Seismic Network) doi: 10.7914/SN/XI_2000

Nyblade, A. A. (2007). *AfricaArray.* International Federation of Digital Seismograph Networks. (Seismic Network) doi: 10.7914/SN/ZP_2007

Ogden, C. S., Bastow, I. D., Gilligan, A., & Rondenay, S. (2019). A reappraisal of the H–κ stacking technique: implications for global crustal structure. *Geophys. J. Int.*, *219*(3), 1491–1513. doi: 10.1093/gji/ggz364

Owens, T. J., & Nyblade, A. A. (1994). *Seismic investigations of the Lithospheric Structure of the Tanzanian Craton.* International Federation of Digital Seismograph Networks. (Seismic Network) doi: 10.7914/SN/XD_1994

O'Donnell, J. P., Adams, A. N., Nyblade, A. A., Mulibo, G. D., & Tugume, F. (2013). The uppermost mantle shear wave velocity structure of eastern Africa from Rayleigh wave tomography: constraints on rift evolution. *Geophys. J. Int.*, *194*(2), 961–978. doi: 10.1093/gji/ggt135

Pasyanos, M. E., & Nyblade, A. A. (2007). A top to bottom lithospheric study of Africa and Arabia. *Tectonophysics*, *444*(1-4), 27–44. doi: 10.1016/j.tecto.2007 .07.008

Penn State University. (2004). *AfricaArray.* International Federation of Digital Seismograph Networks. (Seismic Network) doi: 10.7914/SN/AF

Pik, R., Marty, B., Carignan, J., & Lavé, J. (2003). Stability of the Upper Nile drainage network (Ethiopia) deduced from (U–Th)/He thermochronometry:

implications for uplift and erosion of the Afar plume dome. *Earth Planet. Sci. Lett.*, *215*(1-2), 73–88. doi: 10.1016/s0012-821x(03)00457-6

Pik, R., Marty, B., Carignan, J., Yirgu, G., & Ayalew, T. (2008). Timing of East African Rift development in southern Ethiopia: Implication for mantle plume activity and evolution of topography. *Geology*, *36*(2), 167–170. doi: 10.1130/g24233a.1

Pik, R., Marty, B., & Hilton, D. (2006). How many mantle plumes in Africa? The geochemical point of view. *Chemical Geology*, *226*(3-4), 100–114. doi: 10.1016/j.chemgeo.2005.09.016

Pratt, M. J., Wysession, M. E., Aleqabi, G., Wiens, D. A., Nyblade, A. A., Shore, P., ... Rindraharisaona, E. (2017). Shear velocity structure of the crust and upper mantle of Madagascar derived from surface wave tomography. *Earth Planet. Sci. Lett.*, *458*, 405–417. doi: 10.1016/j.epsl.2016.10.041

Priestley, K., McKenzie, D., Debayle, E., & Pilidou, S. (2008). The African upper mantle and its relationship to tectonics and surface geology. *Geophys. J. Int.*, *175*(3), 1108–1126. doi: 10.1111/j.1365-246x.2008.03951.x

Priestley, K., McKenzie, D., & Ho, T. (2019). A Lithosphere - Asthenosphere Boundary - a Global Model Derived from Multimode Surface-Wave Tomography and Petrology. In H. Yuan & B. Romanowicz (Eds.), *Lithospheric discontinuities* (1st ed., Vols. Geophysical Monograph, 239, pp. 111–123). American Geophysical Union and John Wiley & Sons, Inc. doi: 10.1002/9781119249740

Rajaonarison, T. A., Stamps, D. S., Fishwick, S., Brune, S., Glerum, A., & Hu, J. (2020). Numerical Modeling of Mantle Flow Beneath Madagascar to Constrain Upper Mantle Rheology Beneath Continental Regions. *J. Geophys. Res.*, *125*(2). doi: 10.1029/2019jb018560

Reed, C. A., Gao, S. S., Liu, K. H., & Yu, Y. (2016). The mantle transition zone beneath the Afar Depression and adjacent regions: implications for mantle plumes and hydration. *Geophys. J. Int.*, *205*(3), 1756–1766. doi: 10.1093/gji/ggw116

Reusch, A. M., Nyblade, A. A., Tibi, R., Wiens, D. A., Shore, P. J., Bekoa, A., ... Nnange, J. M. (2011). Mantle transition zone thickness beneath Cameroon: evidence for an upper mantle origin for the Cameroon Volcanic Line. *Geophys. J. Int.*, *187*(3), 1146–1150. doi: 10.1111/j.1365-246x.2011.05239.x

Reusch, A. M., Nyblade, A. A., Wiens, D. A., Shore, P. J., Ateba, B., Tabod, C. T., & Nnange, J. M. (2010). Upper mantle structure beneath Cameroon from body wave tomography and the origin of the Cameroon Volcanic Line. *Geochem. Geophys. Geosyst.*, *11*(10), Q10W07. doi: 10.1029/2010gc003200

Ritsema, J., Deuss, A., Van Heijst, H., & Woodhouse, J. (2011). S40RTS: a degree-40 shear-velocity model for the mantle from new Rayleigh wave dispersion, teleseismic traveltime and normal-mode splitting function measurements. *Geophys. J. Int.*, *184*(3), 1223–1236. doi: 10.1111/j.1365-246X.2010.04884.x

Ritsema, J., & Van Heijst, H. (2000). New seismic model of the upper mantle beneath Africa. *Geology*, *28*(1), 63-66. doi: 10.1130/0091-7613(2000)28⟨63:NSMOTU⟩2.0.CO;2

Ritsema, J., Van Heijst, H., & Woodhouse, J. (1999). Complex shear wave velocity structure imaged beneath Africa and Iceland. *Science*, *286*, 1925-1928. doi: 10.1126/science.286.5446.1925

Rogers, N. W., Davies, M. K., Parkinson, I. J., & Yirgu, G. (2010). Osmium isotopes and Fe/Mn ratios in Ti-rich picritic basalts from the Ethiopian flood basalt province: No evidence for core contribution to the Afar plume. *Earth Planet. Sci. Lett.*, *296*(3-4), 413–422. doi: 10.1016/j.epsl.2010.05.027

Rogers, N. W., Macdonald, R., Fitton, J., George, R., Smith, R., & Barreiro, B. (2000). Two mantle plumes beneath the East African rift system: Sr, Nd and Pb isotope evidence from Kenya Rift basalts. *Earth Planet. Sci. Lett.*, *176*, 387-400. doi: 10.1016/s0012-821x(00)00012-1

Rooney, T. O. (2017). The Cenozoic magmatism of East-Africa: Part I — Flood basalts and pulsed magmatism. *Lithos*, *286-287*, 264 - 301. doi: https://doi.org/10.1016/j.lithos.2017.05.014

Rooney, T. O. (2020a). The Cenozoic magmatism of East Africa: Part II – Rifting of the mobile belt. *Lithos*, *360-361*, 105291. doi: https://doi.org/10.1016/j.lithos.2019.105291

Rooney, T. O. (2020b). The Cenozoic magmatism of East Africa: Part V – Magma sources and processes in the East African Rift. *Lithos*, *360-361*, 105296. doi: https://doi.org/10.1016/j.lithos.2019.105296

Rooney, T. O., Herzberg, C., & Bastow, I. D. (2012). Elevated mantle temperature beneath East Africa. *Geology*, *40*(G32382R1), 27-40. doi: 10.1130/G32382.1

Rudnick, R. L., McDonough, W. F., & Chappell, B. W. (1993). Carbonatite metasomatism in the northern Tanzanian mantle: Petrographic and geochemical characteristics. *Earth Planet. Sci. Lett.*, *114*(4), 463–475. doi: 10.1016/0012-821x(93)90076-l

Saria, E., Calais, E., Stamps, D. S., Delvaux, D., & Hartnady, C. J. H. (2014). Present-day kinematics of the East African Rift. *J. Geophys. Res.*, *119*(4), 3584–3600. doi: 10.1002/2013jb010901

Schutt, D. L., & Lesher, C. E. (2006). Effects of melt depletion on the density and seismic velocity of garnet and spinel lherzolite. *J. Geophys. Res.*, *111*(B5). doi: 10.1029/2003JB002950

Schutt, D. L., & Lesher, C. E. (2010). Compositional trends among Kaapvaal Craton garnet peridotite xenoliths and their effects on seismic velocity and density. *Earth Planet. Sci. Lett.*, *300*(3-4), 367–373. doi: 10.1016/j.epsl.2010.10.018

Sepulchre, P., Ramstein, G., Fluteau, F., Schuster, M., Tiercelin, J., & Brunet, M. (2006). Tectonic uplift and Eastern Africa aridification. *Science*, *313*(5792), 1419–1423. doi: 10.1126/science.1129158

Silver, P. G. (1997). *A Multidisciplinary Experiment across the Kaapvaal Craton.* International Federation of Digital Seismograph Networks. (Seismic Network) doi: 10.7914/SN/XA_1997

Simmons, N. A., Forte, A. M., & Grand, S. P. (2007). Thermochemical structure and dynamics of the African superplume. *Geophys. Res. Lett.*, *34*(2). doi: 10.1029/2006GL028009

Simmons, N. A., Myers, S. C., Johannesson, G., & Matzel, E. (2012). LLNL-G3Dv3: Global P wave tomography model for improved regional and teleseismic travel time prediction. *J. Geophys. Res.*, *117*(B10). doi: 10.1029/2012jb009525

Stachel, T., Harris, J. W., & Brey, G. P. (1998). Rare and unusual mineral inclusions in diamonds from Mwadui, Tanzania. *Contributions to Mineralogy and Petrology*, *132*(1), 34–47. doi: 10.1007/s004100050403

Steinberger, B., & Torsvik, T. H. (2012). A geodynamic model of plumes from the margins of Large Low Shear Velocity Provinces. *Geochem. Geophys. Geosyst.*, *13*(1). doi: 10.1029/2011gc003808

Suh, C., Ayonghe, S., Sparks, R., Annen, C., Fitton, J., Nana, R., & Luckman, A. (2003). The 1999 and 2000 Eruptions of Mount Cameroon: Eruption Behaviour and Petrochemistry of Lava. *Bulletin of volcanology*, *65*(4), 267–281. doi: 10.1007/s00445-002-0257-7

Tappe, S., Smart, K., Torsvik, T., Massuyeau, M., & de Wit, M. (2018). Geodynamics of kimberlites on a cooling Earth: Clues to plate tectonic evolution and deep volatile cycles. *Earth Planet. Sci. Lett.*, *484*, 1–14. doi: 10.1016/j.epsl.2017.12.013

Thomas, C. (2010). *Morocco-Muenster.* International Federation of Digital Seismograph Networks. (Seismic Network) doi: 10.7914/SN/3D_2010

Thompson, D. A., Hammond, J. O. S., Kendall, J., Stuart, G. W., Helffrich, G. R., Keir, D., ... Goitom, B. (2015). Hydrous upwelling across the mantle transition zone beneath the Afar Triple Junction. *Geochem. Geophys. Geosyst.*,

16(3), 834–846. doi: 10.1002/2014gc005648

Tilmann, F., Yuan, X., Rümpker, G., & Rindraharisaona, E. (2012). *SELASOMA Project, Madagascar 2012-2014.* Deutsches GeoForschungsZentrum GFZ. (Seismic Network) doi: 10.14470/MR7567431421

Utrecht University (UU Netherlands). (1983). *NARS.* International Federation of Digital Seismograph Networks. (Seismic Network) doi: 10.7914/SN/NR

VanDecar, J., & Crosson, R. (1990). Determination of teleseismic relative phase arrival times using multi-channel cross-correlation and least squares. *Bull. Seis. Soc. Am.*, *80*(1), 150-169.

Velasco, A., & Kaip, G. (2011). *Seismic Characterization of Menengai Crater, Kenya.* International Federation of Digital Seismograph Networks. (Seismic Network) doi: 10.7914/SN/1C_2011

Vergne, J., Doubre, C., & Leroy, S. (2014). *Seismic network 7c:dora experiment (resif-sismob).* RESIF - Réseau Sismologique et géodésique Français. (Seismic Network) doi: 10.15778/RESIF.7C2009

Vernon, F., & James, D. (1998). *Broad Band Array Study in South Africa.* International Federation of Digital Seismograph Networks. (Seismic Network) doi: 10.7914/SN/YB_1998

Vigny, C., Huchon, P., Ruegg, J.-C., Khanbari, K., & Asfaw, L. M. (2006). Confirmation of Arabia plate slow motion by new GPS data in Yemen. *J. Geophys. Res.*, *111*(B2). doi: 10.1029/2004jb003229

Wagner, L. S., Anderson, M. L., Jackson, J. M., Beck, S. L., & Zandt, G. (2008). Seismic evidence for orthopyroxene enrichment in the continental lithosphere. *Geology*, *36*, 935–938. doi: 10.1130/g25108a.1

Wang, H., van Hunen, J., & Pearson, D. G. (2015). The thinning of subcontinental lithosphere: The roles of plume impact and metasomatic weakening. *Geochem. Geophys. Geosyst.*, *16*(4), 1156-1171. doi: 10.1002/2015GC005784

Weeraratne, D., Forsyth, D., Fischer, K., & Nyblade, A. (2003). Evidence for an upper mantle plume beneath the Tanzanian craton from Rayleigh wave tomography. *J. Geophys. Res.*, *108*(B9). doi: 10.1029/2002JB002273

Wenker, S., & Beaumont, C. (2018). Can metasomatic weakening result in the rifting of cratons? *Tectonophysics*, *746*, 3-21. doi: 10.1016/j.tecto.2017.06.013

White, R., & McKenzie, D. (1989). Magmatism at rift zones: the generation of volcanic continental margins and flood basalts. *J. Geophys. Res.*, *94*, 7685-7729.

Wichura, H., Bousquet, R., Oberhänsli, R., Strecker, M. R., & Trauth, M. H. (2010). Evidence for middle Miocene uplift of the East African Plateau. *Geology*, *38*(6), 543–546. doi: 10.1130/G31022.1

Wiens, D. A., & Nyblade, A. A. (2005). *Broadband Seismic Investigation of the Cameroon Volcanic Line.* International Federation of Digital Seismograph Networks. (Seismic Network) doi: 10.7914/SN/XB_2005

Williams, C. D., Li, M., McNamara, A. K., Garnero, E. J., & van Soest, M. C. (2015). Episodic entrainment of deep primordial mantle material into ocean island basalts. *Nature Communications*, *6*(1), 8937. doi: 10.1038/ncomms9937

Williams, C. D., Mukhopadhyay, S., Rudolph, M. L., & Romanowicz, B. (2019). Primitive Helium Is Sourced From Seismically Slow Regions in the Lowermost Mantle. *Geochem. Geophys. Geosyst.*, *20*(8), 4130–4145. doi: 10.1029/2019gc008437

Wölbern, I., Rümpker, G., Link, K., & Sodoudi, F. (2012). Melt infiltration of the lower lithosphere beneath the Tanzania craton and the Albertine rift inferred from S receiver functions. *Geochem. Geophys. Geosyst.*, *13*(8). doi: 10.1029/2012gc004167

Woolley, A. R., & Kjarsgaard, B. A. (2008). *Carbonatite Occurrences of the World: Map and Database; Geological Survey of Canada, Open File 5796.* (data retrieved from Natural Resources Canada, `https://geoscan.nrcan.gc.ca/starweb/geoscan/servlet.starweb?path=geoscan/fulle.web&search1=R=`

225115) doi: 10.4095/225115

Wysession, M. E., Wiens, D. A., & Nyblade, A. A. (2011). *Investigation of sources of intraplate volcanism using PASSCAL broadband instruments in Madagascar, The Comores, and Mozambique.* International Federation of Digital Seismograph Networks. (Seismic Network) doi: 10.7914/SN/XV_2011

Youssof, M., Thybo, H., Artemieva, I., & Levander, A. (2015). Upper mantle structure beneath southern African cratons from seismic finite-frequency P- and S-body wave tomography. *Earth Planet. Sci. Lett.*, *420*, 174-186. doi: 10.1016/j.epsl.2015.01.034

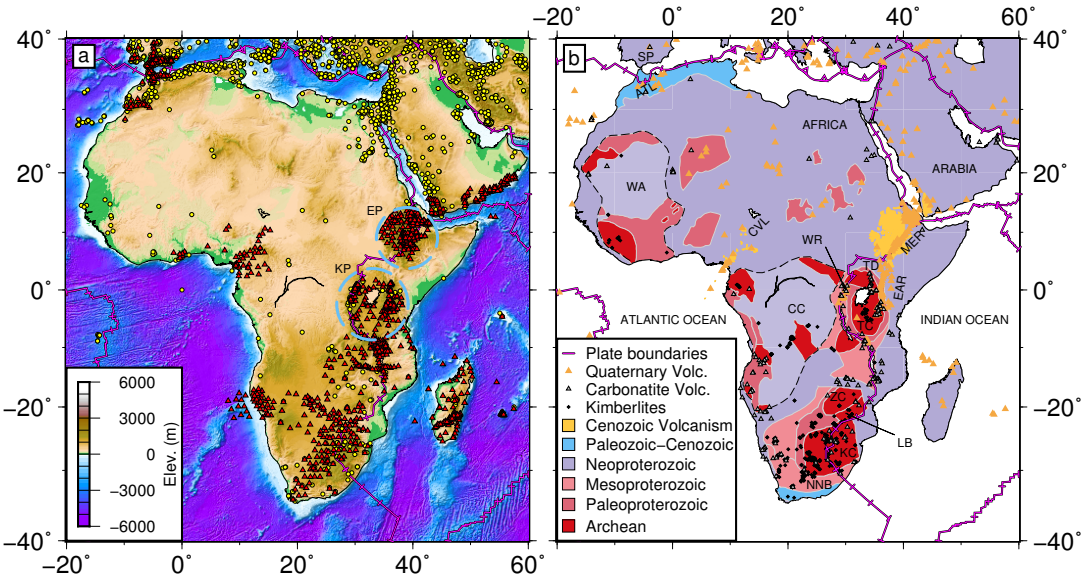

Figure 1. (*a*) Yellow circles: stations included in the "EHB" database (Engdahl et al., 1998). Red triangles: 1994–2019 temporary seismograph station deployments from which absolute arrival-times are obtained via the method of Boyce et al. (2017). Magenta lines: plate boundaries. Light blue dashed circles: the Ethiopian (EP) and Kenyan (KP) topographic plateaus. (*b*) African crustal geology after Begg et al. (2009). Transparent regions with black dashed outline mark inferred craton extents, presently covered by Phanerozoic sediments. Orange triangles: Quaternary volcanoes. Gray triangles: Carbonatite volcanoes (Woolley & Kjarsgaard, 2008). Black diamonds: kimberlites (Tappe et al., 2018). Yellow regions: Cenozoic volcanic provinces. ATL: Atlas Mountains CC: Congo Craton, CVL: Cameroon Volcanic Line, EAR: East African Rift, KC: Kaapvaal Craton, LB: Limpopo belt, MER: Main Ethiopian rift, NNB: Namaqua-Natal belt, SP: Spain, TC: Tanzanian Craton, TD: Turkana Depression, WA: West African Craton, WR: Western Rift, ZC: Zimbabwe Craton.

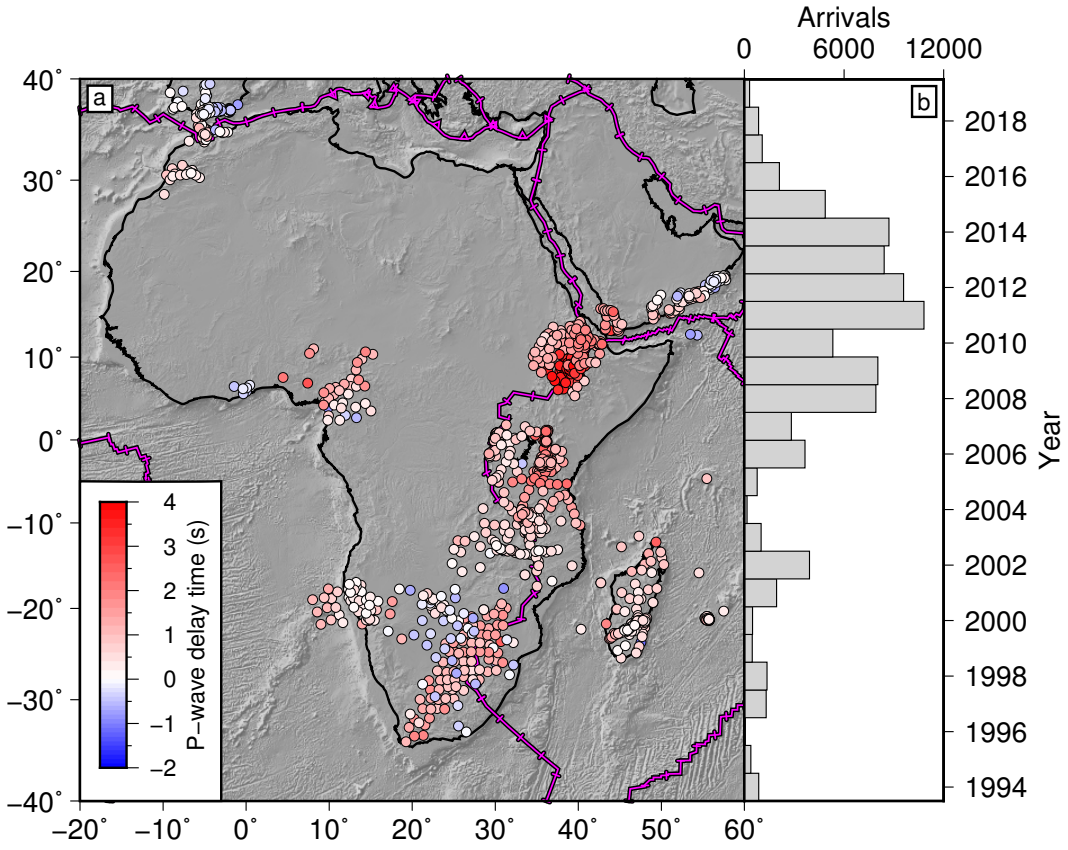

Figure 2. (*a*) Mean absolute arrival-time residuals for temporary seismic stations across Africa calculated using AARM (Boyce et al., 2017) with respect to ak135 (Kennett et al., 1995). Negative residuals are early arrivals (fast); positive residuals are late arrivals (slow). Residuals are corrected for station elevation and plotted on an asymmetric color bar from +4 s to −2 s delay time. Magenta lines: plate boundaries. (*b*) Histogram of residuals binned by year.

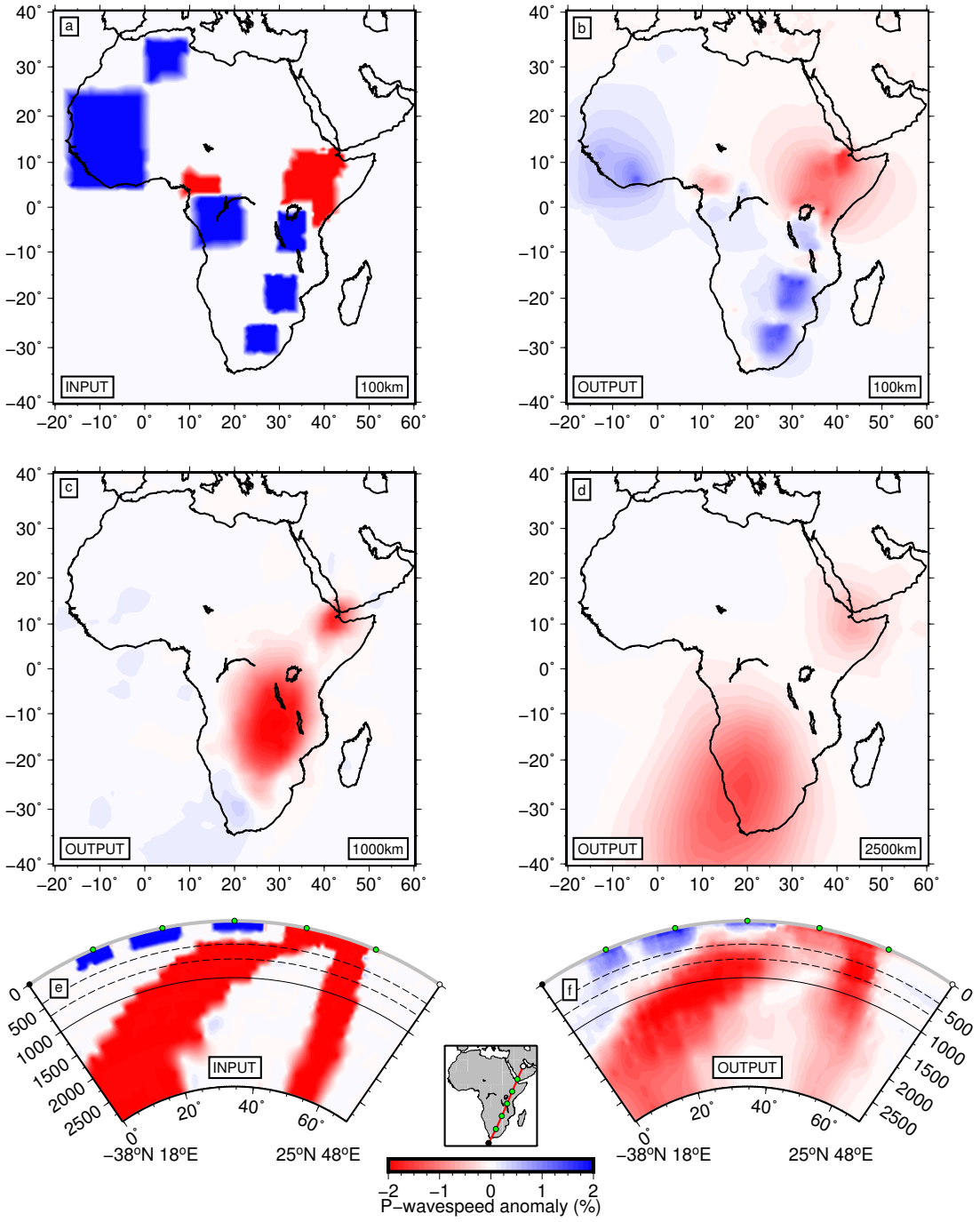
a
INPUT
100km
b
OUTPUT
100km
c
OUTPUT
1000km
d
OUTPUT
2500km
e
INPUT
f
OUTPUT
0
500
1000
1500
2000
2500
20°
40°
60°
−38°N 18°E
25°N 48°E
−2 −1 0 1 2
P−wavespeed anomaly (%)

Figure 3. An inclined, elliptical, input slow wavespeed anomaly (δV_P = –2.0%) increases in areal extent from the surface, centered at 10°N, 40°E, to the core-mantle boundary, centered at 35°S, 15°E (*a,e*). We also add a narrower planform, more steeply dipping slow wavespeed anomaly (δV_P = –2.0%) extending from the surface, centered at 10°N, 42°E, to the core-mantle boundary, centered at 13°N, 44°E (*a,e*). We insert δV_P = +2% wavespeed anomalies as cratonic cores in the upper 270 km in west Africa, Congo and southern Africa and the upper 180 km in Tanzania. We insert a δV_P = –2% wavespeed anomaly below the Cameroon Volcanic Line to 270 km depth (*a,e*). We ensure that input whole-mantle slow wavespeed anomalies do not overlap upper mantle input anomalies using a δV_P = 0% buffer region. Visual defects within the input anomaly model result from a coarse adaptive grid in poorly sampled regions. The cross-section location is indicated in the inset map between *e* and *f*. Recovered anomalies, shown at 100 km, 1000 km, 2500 km depth and in cross-section (*b–d,f*) are displayed on the same color scale as the input.

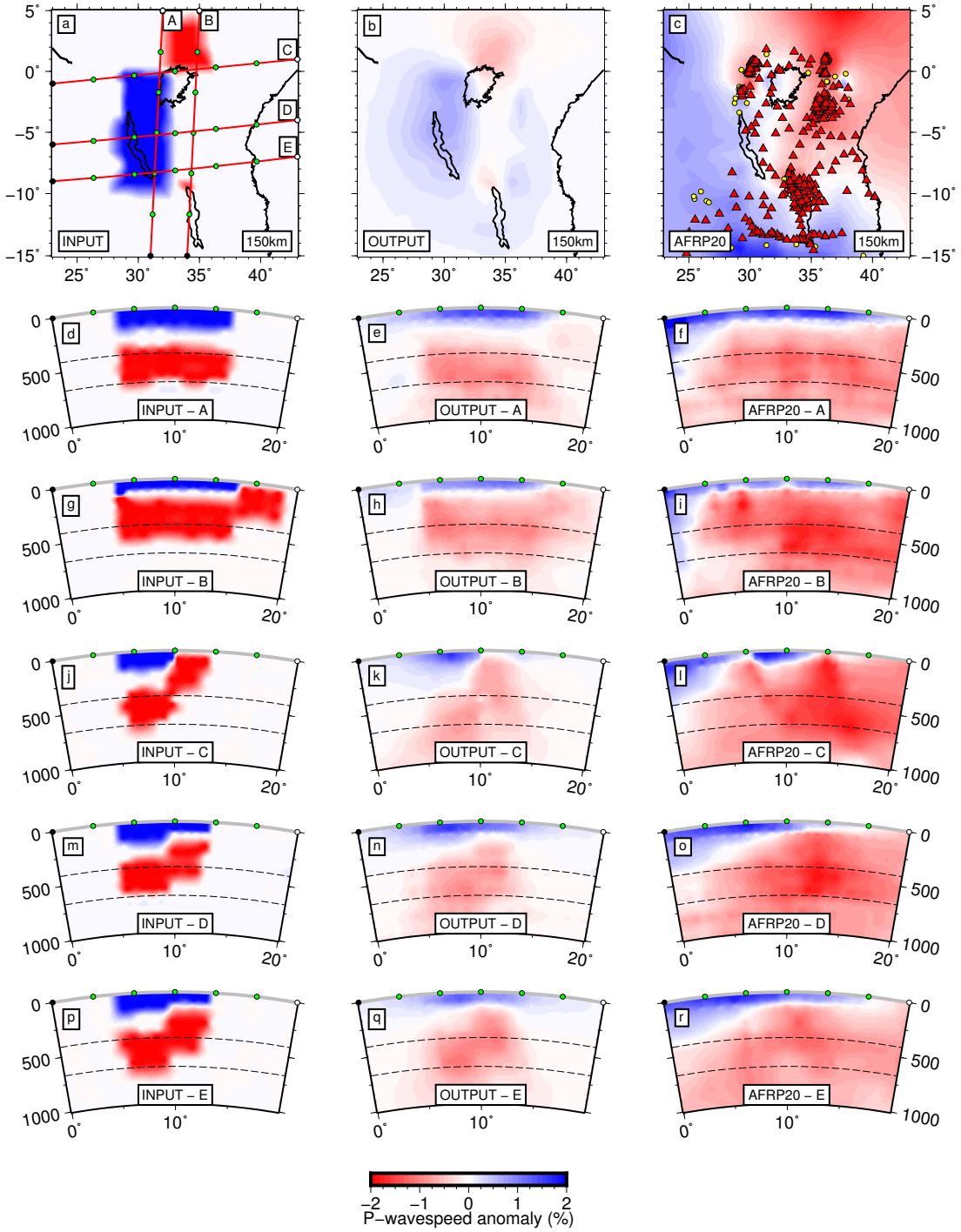
a
A
B
C
D
E
INPUT
150km
b
OUTPUT
150km
c
AFRP20
150km
5˚
0˚
−5˚
−10˚
−15˚
25˚
30˚
35˚
40˚
d
INPUT – A
e
OUTPUT – A
f
AFRP20 – A
g
INPUT – B
h
OUTPUT – B
i
AFRP20 – B
j
INPUT – C
k
OUTPUT – C
l
AFRP20 – C
m
INPUT – D
n
OUTPUT – D
o
AFRP20 – D
p
INPUT – E
q
OUTPUT – E
r
AFRP20 – E
0
500
1000
0˚
10˚
20˚
−2
−1
0
1
2
P−wavespeed anomaly (%)

Figure 4. To test the sensitivity of AFRP20 to complex upper mantle wavespeed structure below Tanzania, we insert a rectangular (9–0°S, 30–36°E) fast wavespeed anomaly in the upper mantle below Tanzania ($\delta V_P = +2.0\%$). This anomaly extends to 180 km depth in the west and 135 km in the east. We arrange a series of slow wavespeed anomalies ($\delta V_P = -2\%$) as follows: a shallow (50–300 km depth) anomaly centered at ∼2°N, 35°E to the northeast of the Tanzanian craton, a tabular anomaly below the eastern Tanzanian craton (150–550 km depth) and a tabular anomaly below the western Tanzanian craton at greater depths (410–660 km depth). Visual defects within the input anomaly model result from a coarse adaptive grid in poorly sampled regions. The cross-section locations (A–E) are indicated in *a*. Yellow circles and red triangles on map (*c*) show the locations of "EHB" stations and temporary deployments analyzed in this study. The test input (*a,d,g,j,m,p*), output (*b,e,h,k,n,q*) and AFRP20 (*c,f,i,l,o,r*) are displayed on the same color scale.

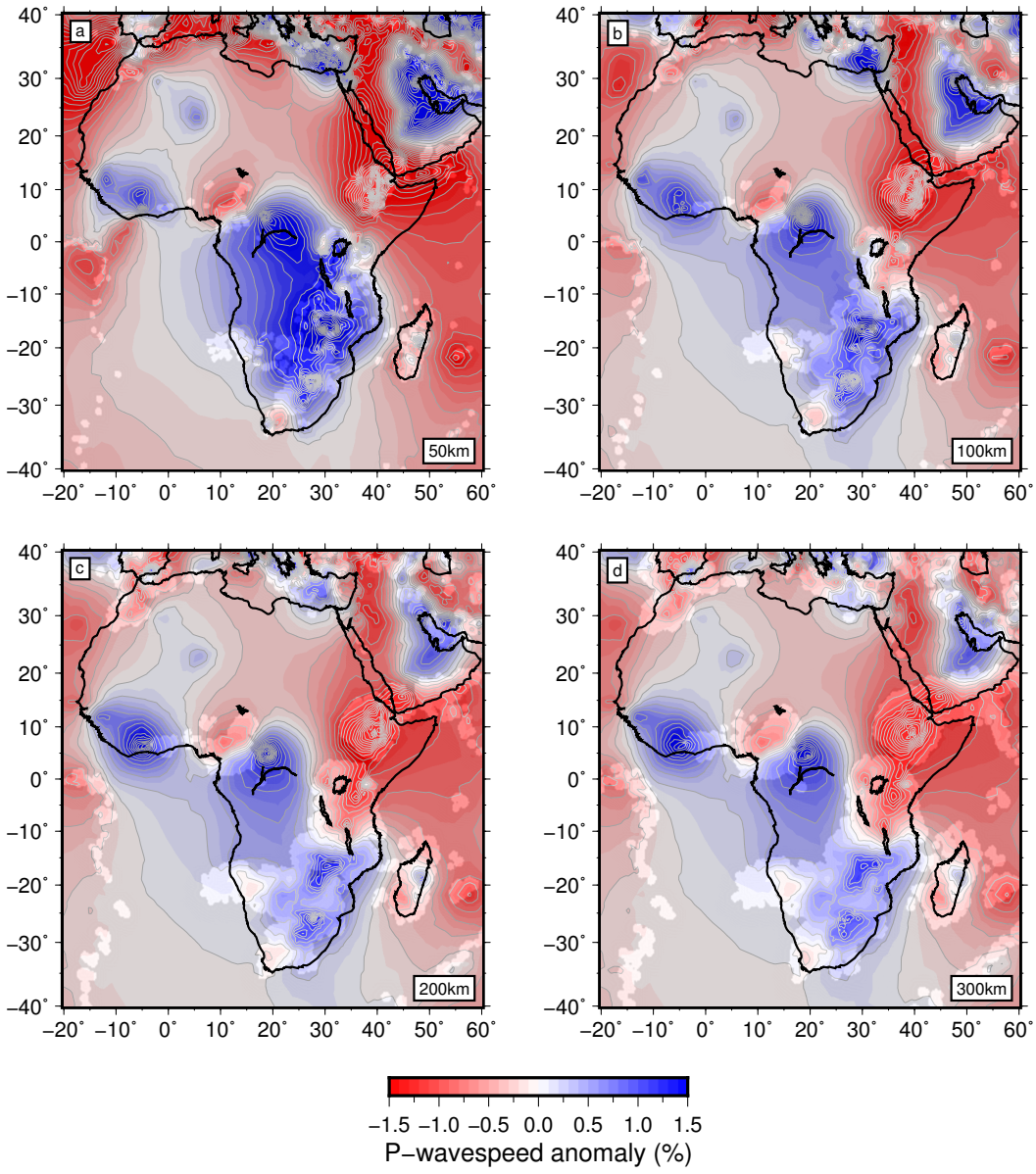

Figure 5. AFRP20 African tomographic model at upper mantle depths of 50 km, 100 km, 200 km and 300 km (*a*-*d*) plotted as percentage deviation from ak135 (δV_P=±1.5%). Gray regions are not constrained by our new AARM-derived African data set (see Supplementary Material), only by the global data set (Li et al., 2008). Particularly at these upper mantle depths, resolution offered by the global data set is limited to regions of high earthquake and station density (Figures S1–S2, S27–S31).

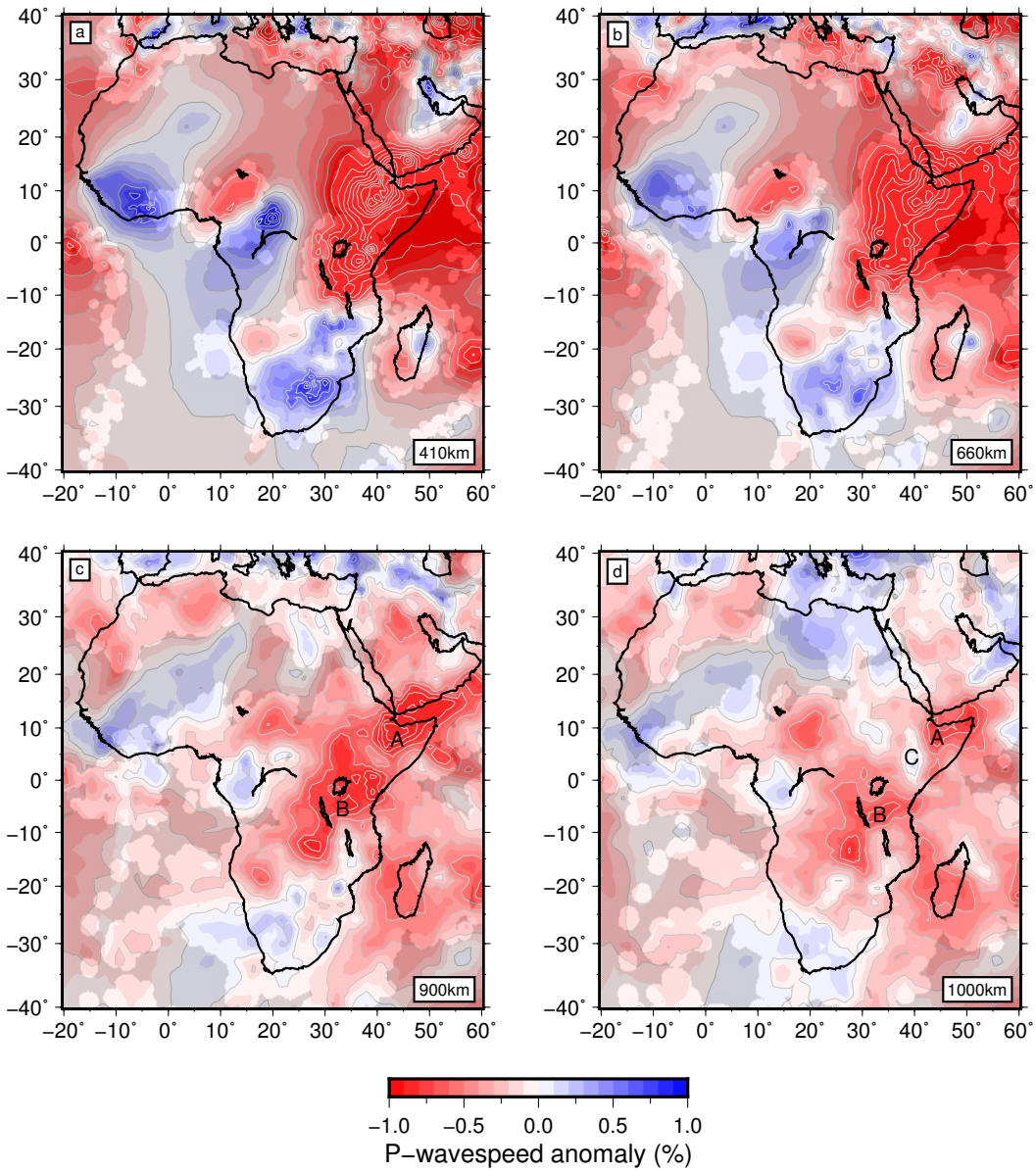

Figure 6. AFRP20 African tomographic model at mid-mantle depths of 410 km, 660 km, 900 km and 1000 km (*a*-*d*) plotted as percentage deviation from ak135 (δV_P=±1%). Gray regions are not constrained by our new AARM-derived African data set (see Supplementary Material), only by the global data set (Li et al., 2008).

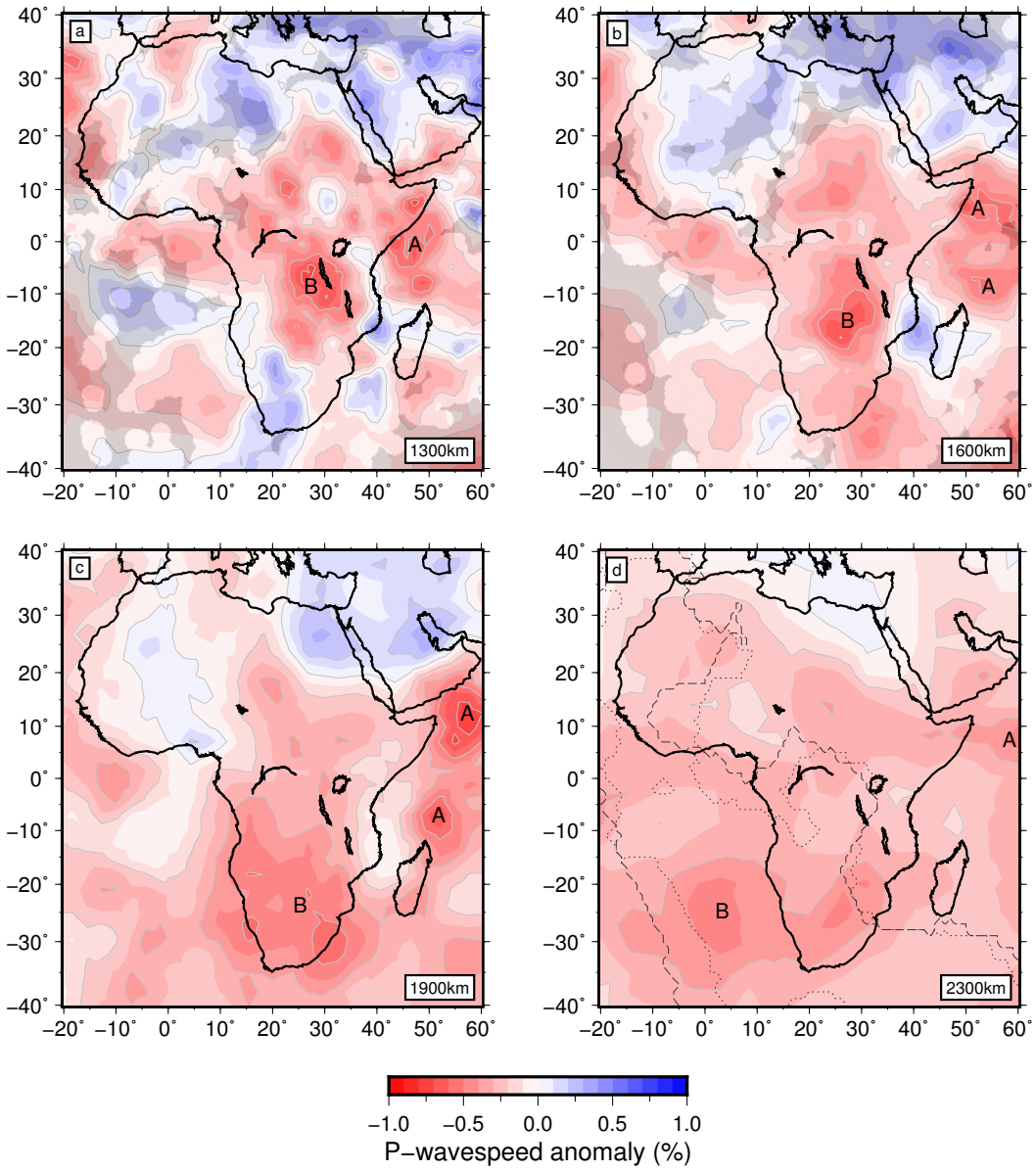

Figure 7. AFRP20 African tomographic model at lower mantle depths of 1300 km, 1600 km, 1900 km and 2300 km (*a*-*d*) plotted as percentage deviation from ak135 (δV_P=±1%). Gray regions are not constrained by our new AARM-derived African data set (see Supplementary Material), only by the global data set (Li et al., 2008). Within subplot (*d*), dashed and dotted dark gray lines mark regions of 5/5 slow-wavespeed votes near the core-mantle boundary in δV_S and δV_P tomographic models respectively, clustered by Cottaar and Lekić (2016). Anomaly B lies inside these contours while anomaly A lies outside.

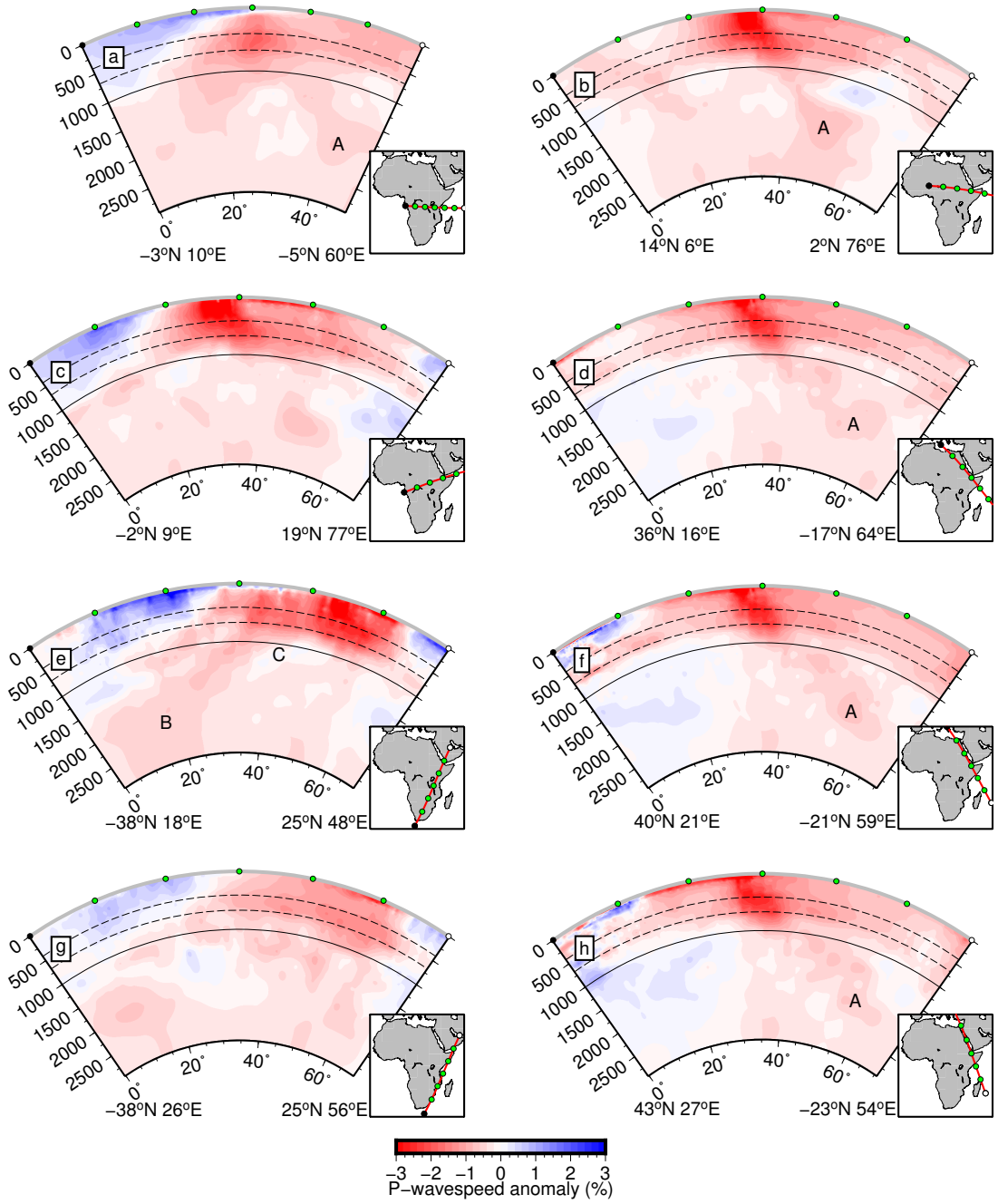

Figure 8. AFRP20 African tomographic model on several cross-sections (*a-h*) indicated by each inset map subfigure, plotted as percentage deviation from ak135 (δV_P=±3%).

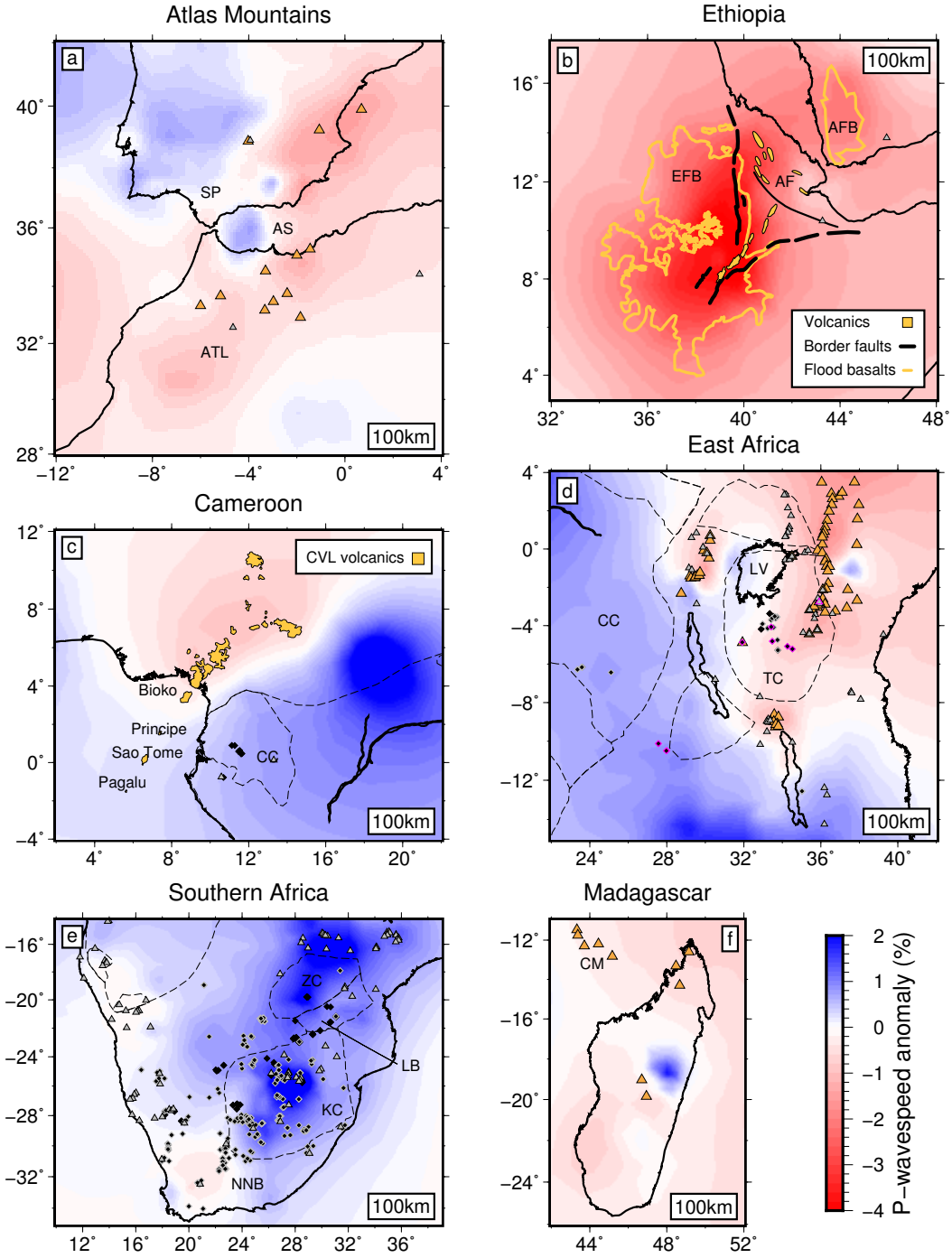
Atlas Mountains
a
SP
AS
ATL
100km
Ethiopia
b
100km
AFB
EFB
AF
Volcanics
Border faults
Flood basalts
Cameroon
c
CVL volcanics
Bioko
Principe
Sao Tome
Pagalu
CC
100km
East Africa
d
LV
CC
TC
100km
Southern Africa
e
ZC
LB
KC
NNB
100km
Madagascar
f
CM
100km
P−wavespeed anomaly (%)

Figure 9. (*a-f*) P-wavespeeds at 100 km depth within each region for which spatial sampling is greatly improved by the addition of new AARM-derived absolute arrival-times (Figure 2). Orange triangles: Quaternary volcanoes. Gray triangles: Carbonatite volcanoes; the only active Carbonatite volcano at Ol Doinyo Lengai, Tanzania is outlined pink (Woolley & Kjarsgaard, 2008). Black diamonds: kimberlite locations; those erupted since 500 Ma and 50 Ma are outlined in gray and pink, respectively (Tappe et al., 2018). Yellow regions: Cenozoic volcanic provinces. Black dashed polygons: the craton outlines shown in Figure 1. AF: Afar depression, AFB: Arabian flood basalts, AS: Alboran Sea, CM: Comoros and Mayote, EFB: Ethiopian flood basalts, LV: Lake Victoria. Other acronyms follow Figure 1. Wavespeed plotted as percentage deviation from ak135 on an asymmetric color scale ($-4\% \leq \delta V_P \leq 2\%$) to illuminate the full extent of wavespeed heterogeneity.